

WILEY-VCH

 **Chemistry  
Europe**  
European Chemical  
Societies Publishing

# Take Advantage and Publish Open Access



By publishing your paper open access, you'll be making it immediately freely available to anyone everywhere in the world.

That's maximum access and visibility worldwide with the same rigor of peer review you would expect from any high-quality journal.

**Submit your paper today.**



[www.chemistry-europe.org](http://www.chemistry-europe.org)

# Broad-Spectrum Antidote Discovery by Untangling the Reactivation Mechanism of Nerve-Agent-Inhibited Acetylcholinesterase

Cecilia Lindgren,<sup>[a]</sup> Nina Forsgren,<sup>[b]</sup> Norman Hoster,<sup>[a]</sup> Christine Akfur,<sup>[b]</sup> Elisabet Artursson,<sup>[b]</sup> Lotta Edvinsson,<sup>[a]</sup> Richard Svensson,<sup>[c]</sup> Franz Worek,<sup>[d]</sup> Fredrik Ekström,<sup>\*,[b]</sup> and Anna Linusson<sup>\*,[a]</sup>

**Abstract:** Reactivators are vital for the treatment of organophosphorus nerve agent (OPNA) intoxication but new alternatives are needed due to their limited clinical applicability. The toxicity of OPNAs stems from covalent inhibition of the essential enzyme acetylcholinesterase (AChE), which reactivators relieve via a chemical reaction with the inactivated enzyme. Here, we present new strategies and tools for developing reactivators. We discover suitable inhibitor scaffolds by using an activity-independent competition assay to

study non-covalent interactions with OPNA-AChEs and transform these inhibitors into broad-spectrum reactivators. Moreover, we identify determinants of reactivation efficiency by analysing reactivation and pre-reactivation kinetics together with structural data. Our results show that new OPNA reactivators can be discovered rationally by exploiting detailed knowledge of the reactivation mechanism of OPNA-inhibited AChE.

## Introduction

Although the chemical weapons convention (CWC)<sup>[1]</sup> prohibits the use of chemical weapons, organophosphorus nerve agents (OPNAs, Figure 1) have been misused on several occasions, resulting in severe human intoxications and many casualties.<sup>[2,3]</sup> OPNAs inhibit the enzyme acetylcholinesterase (AChE), which is essential for the functionality of the nervous system. The loss of AChE activity causes an accumulation of the neurotransmitter acetylcholine, leading to a cholinergic crisis with toxic and

potentially lethal outcomes. Symptomatic interventions for treating nerve agent intoxication include treatment with atropine and various anticonvulsants. In addition, AChE activity can be restored by therapeutic treatment with a reactivator.<sup>[3]</sup> The reactivators used in the clinic are the pyridinium oximes 2-PAM, HI-6, and obidoxime (Figure 1). These drugs are highly valued for treating nerve agent intoxications but their clinical efficacy depends on the OPNA that caused the toxicity, which limits their applicability.<sup>[4]</sup> Furthermore, these agents cannot readily cross the blood brain barrier (BBB), which reduces their therapeutic efficiency because OPNAs cross the BBB and interfere with the central nervous system (CNS).<sup>[5,6]</sup> Consequently, there are ongoing efforts to identify antidotes with broad-spectrum activity against multiple OPNAs. Unfortunately, the complexity of the OPNA-AChE system has hampered the development of improved reactivators and many studies have been hit-or-miss, partly due to a lack of methods to support rational reactivator design.<sup>[7–10]</sup>

Structural studies have shown that AChE has a deep and narrow active site gorge that is lined with aromatic amino acid residues. Three loops at the entrance of the gorge constitute the peripheral site, while the active site with its catalytic triad (Ser203, His447 and Glu334) is located near the bottom of the gorge (Figure 2A).<sup>[11]</sup> OPNAs impair the function of AChE by acting as selective electrophiles that react with the catalytic serine to form a covalent bond (Figure 1) while also forming various non-covalent interactions with other amino acid residues.<sup>[12–16]</sup> The rate of hydrolysis (i.e., the rate of spontaneous AChE reactivation) is low for most OPNA-AChE adducts, so the inhibition of AChE is effectively irreversible. Reactivators carry a nucleophilic oxime functionality that can cleave the bond between the OPNA and AChE, thereby restoring the


[a] Dr. C. Lindgren, N. Hoster, Dr. L. Edvinsson, Prof. A. Linusson  
Department of Chemistry  
Umeå University  
901 87 Umeå (Sweden)  
E-mail: anna.linusson@umu.se

[b] Dr. N. Forsgren, C. Akfur, E. Artursson, Dr. F. Ekström  
CBRN Defense and Security  
Swedish Defense Research Agency  
906 21 Umeå (Sweden)  
E-mail: fredrik.ekstrom@foi.se

[c] Dr. R. Svensson  
Biomedicinskt Centrum BMC  
Uppsala University  
752 37 Uppsala (Sweden)

[d] Dr. F. Worek  
Bundeswehr Institute of Pharmacology and Toxicology  
80937 Munich (Germany)

 Supporting information for this article is available on the WWW under <https://doi.org/10.1002/chem.202200678>

 © 2022 The Authors. Chemistry - A European Journal published by Wiley-VCH GmbH. This is an open access article under the terms of the Creative Commons Attribution Non-Commercial NoDerivs License, which permits use and distribution in any medium, provided the original work is properly cited, the use is non-commercial and no modifications or adaptations are made.

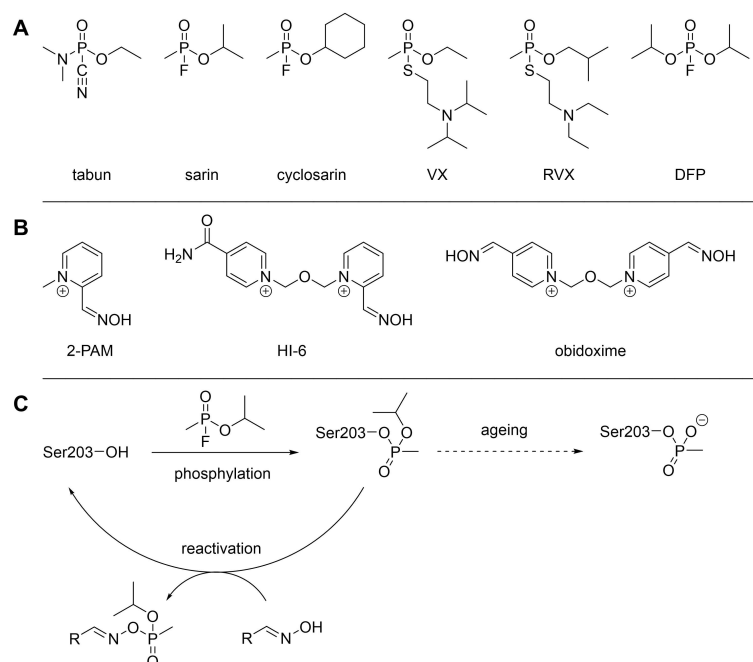


**Figure 1.** A) Chemical structures of selected OPNAs. B) Chemical structures of clinically used reactivators of OPNA inhibited AChE. C) General overview of OPNA inhibition and reactivation of AChE, exemplified with the nerve agent tabun and a general oxime.

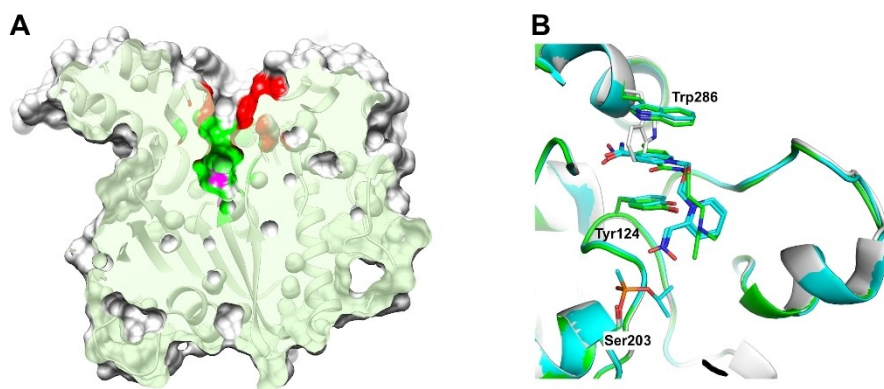


**Figure 2.** A) Intersect of AChE with the catalytic site, the catalytic serine and the binding site of propidium iodide shown in green, magenta and red, respectively. B) Crystal structure of the complex between 1a and mAChE (green, pdb entry code 7R02) superpositioned onto the structure of apo mAChE (gray, pdb entry code 1J06) and the complex between sarin-inhibited mAChE and HI-6 (cyan, pdb entry code 5FFP).

enzyme's activity (Figure 1).<sup>[17]</sup> Oxime reactivators initially bind to the peripheral site of AChE via non-covalent arene-arene interactions, after which the oxime moiety performs a nucleophilic attack on the phosphorus atom of the OPNA adduct, resulting in cleavage of the serine-OPNA covalent bond and reactivation of the enzyme.

Since the discovery of oximes as antidotes to OPNA-inhibited AChE,<sup>[18–21]</sup> great efforts have been made to increase their efficacy and develop broad-spectrum antidotes that can reactivate AChE adducts with diverse OPNAs.<sup>[7,22]</sup> These studies have examined both mono-<sup>[23–27]</sup> and bis-quaternary<sup>[26,28–30]</sup> pyridinium oximes with diverse peripheral site binding scaffolds and variation in the length and chemical composition of the

linker<sup>[26,31–36]</sup> as well as diverse nucleophile-containing moieties.<sup>[37]</sup> There have also been intense efforts to develop oximes that have reactivation capabilities but no permanent charge; such compounds could potentially have superior activity in the CNS.<sup>[38–45]</sup> Other efforts have focused on non-oxime compounds,<sup>[46,47]</sup> fluorinated<sup>[48,49]</sup> and chlorinated species,<sup>[50]</sup> glucose-functionalized compounds,<sup>[51]</sup> prodrugs,<sup>[52]</sup> and bioscavengers.<sup>[53]</sup> However, despite some notable advances and insights into the structure-activity relationships (SARs) of oxime reactivators, progress towards clinically useful new drugs has been limited.

The difficulty of discovering improved antidotes is partly due to the complex mechanism of reactive drugs such as OPNA

antidotes. The residence time of the reversible complex initially formed between the reactivator and the OPNA-AChE adduct must be long enough to permit nucleophilic attack on the phosphorus of the Ser203-OPNA adduct. Furthermore, the reactants (i.e., the oxime oxygen and the phosphorus of the OPNA adduct) involved in the chemical reaction must be positioned in a way that allows sufficient stabilization of the transition state(s) for reactivation to give a clinically useful reaction rate. Finally, the product of the reactivation reaction, (i.e. the phosphorylated reactivator) must leave the reactivated enzyme. The design of broad-spectrum antidotes is further complicated by the fact that the formation of the OPNA-AChE adduct influences the conformations and dynamics of the enzyme's amino acid residues,<sup>[16,54–56]</sup> which in turn affects both the initial reversible binding of the reactivator and the rate of the subsequent chemical reaction.<sup>[4,16,54,57,58]</sup> The difficulty of obtaining structural data on ternary antidote•OPNA-AChE pre-reaction complexes (i.e. Michaelis complexes) presents a further barrier to rational antidote design.<sup>[58]</sup>

Here we apply multiple tools and new strategies to design new reactivators and analyse their SAR in order to better understand the AChE/OPNA/reactivator system and develop more effective strategies for rational design of reactivators. Our approach uses statistical molecular design (SMD), which has previously been employed to study the structure-activity relationships of AChE inhibitors<sup>[59]</sup> and also to a limited extent to investigate reactivators.<sup>[60]</sup> The binding of an SMD-based set of inhibitors to the peripheral sites of OPNA-AChEs is studied using a newly developed biophysical assay in order to identify aromatic scaffolds with broad-spectrum binding profiles. Importantly, this assay is independent of enzymatic activity, which expands the scope of the screening process because it avoids the need for a functional enzyme.<sup>[16]</sup> We then elaborate these scaffolds into a small set of reactivators whose kinetics are characterized in detail. This is important because variables reflecting the strength of enzyme-ligand interactions under steady-state conditions such as the half-maximal inhibitory concentration ( $IC_{50}$ ) and the dissociation constant ( $K_D$ ) provide no information on the rate at which the binding equilibrium is reached or the target residence time ( $\tau$ ) of the binary complex.<sup>[61]</sup> Binding kinetics and the target residence time have received increasing attention in drug discovery in recent years as the potential benefits of drug-target complexes with long half-lives have been recognized.<sup>[62]</sup> The binding kinetics of AChE ligands have been studied previously<sup>[63,64]</sup> but our knowledge of the kinetics of binding and unbinding of oximes to OPNA-AChEs is limited and the utility of  $\tau$  in the design and discovery of reactivators is unexplored. Herein, we report our studies on a new set of antidotes specifically designed to facilitate in-depth analysis by several complementary kinetic and structural methods, including approaches not previously applied in research on nerve agent antidotes.

## Results

### Identification of aromatic scaffolds binding to AChE's peripheral site

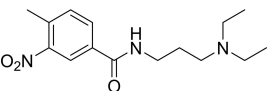
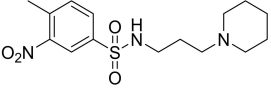
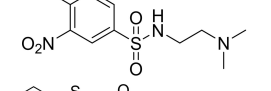
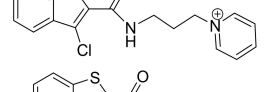
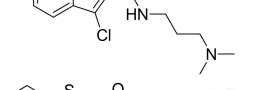
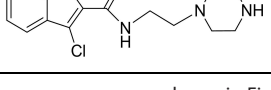
We set out to identify new aromatic scaffolds that bind to the entrance of the active site gorge of a set of OPNA-inhibited AChEs based on the hypothesis that a scaffold with a broad-spectrum binding profile to the peripheral site could serve as a structural template for a broad-spectrum reactivator. To identify such scaffolds, we used a set of 18 compounds previously developed by us to establish quantitative structure-activity relationship (QSAR) models.<sup>[59]</sup> Six different aromatic fragments (Scaffolds 1–6, Figure S1) binding to the peripheral site and six fragments binding to the catalytic site were included in a statistical molecular design (SMD). Two linkers with lengths of two and three carbon atoms were also included in the design. A set of 18 potential AChE inhibitors comprising compounds **1a–c**, **2a–c**, **3a–d**, **4a–c**, **5a–c**, and **6a–b** was obtained by systematically varying these structural fragments (Table 1 and Table S1).

To evaluate the molecules' binding to OPNA-AChE species, we used our previously reported activity-independent competition assay,<sup>[16,59]</sup> in which time-correlated single photon counting (TCSPC) is used to measure the molecules' ability to displace the entrance-binding fluorescent probe propidium iodide (Figure 2A, and Tables 1 and S1). Since the assay does not depend on a catalytically active AChE, the measurements can be performed on both apo AChE and OPNA-AChE species. The new compounds' binding to OPNA-AChE could thus be determined in dose-response experiments. Due to the long duration of the measurements (up to 10 h), this assay is unsuitable for OPNAs with high rates of dealkylation (i.e., ageing, Figure 1) such as sarin and soman. We therefore focused on AChE species of the slow-ageing OPNAs tabun, VX, and RVX. We also included DFP, an organophosphate that is frequently used as a less potent OPNA surrogate.

Analysis of the molecules' binding data revealed that the 4-methyl-3-nitrobenzamide scaffold of compound **1a** and the 3-chlorobenzo[b]thiophene scaffold of compound **2a** showed broad-spectrum binding affinity: compounds containing these fragments displaced propidium iodide in every studied AChE species except DFP-AChE (Figure S2, and Tables 1 and S1). The half-maximal effective concentration ( $EC_{50}$  values for **1a** varied between 6.3 and 27  $\mu$ M (i.e., by a factor of 4), while those for **2a** varied between 9.1 and 47  $\mu$ M (i.e., by a factor of 5). These scaffolds were previously found to have inhibitory potency towards apo AChE.<sup>[59]</sup>

Several of the TCSPC measurements yielded incomplete dose-response curves (e.g. **1c** and **2c**, Figure S2) or artefacts that became noticeable at compound concentrations of 1 mM and above. Furthermore, as expected, some of the compounds (e.g. **4c** and **5c**, Figure S2) did not bind apo AChE or displace propidium iodide from the inhibited enzymes at the tested concentrations. It was therefore impossible to determine accurate  $EC_{50}$  values for these compounds, making the dataset unsuitable for QSAR modelling. The differences in the com-

**Table 1.** Chemical structures and IC<sub>50</sub> and EC<sub>50</sub> values for selected compounds.<sup>[a]</sup>

	Chemical structure	IC <sub>50</sub> Ellman [ $\mu$ M] <sup>[b]</sup> apo hAChE	EC <sub>50</sub> TCSPC [ $\mu$ M]				
			apo hAChE	tabun-hAChE	VX-hAChE	RVX-hAChE	
1a		13 (11–15) <sup>[c]</sup>	27 (21–37)	6.3 (4.9–8.2)	11 (7.0–43)	24 (15–81)	> 500
1b		101 (83–123)	32 (23–69)	14 (9.8–20)	28 (18–137)	26 (19–49)	> 500
1c		70 (55–89)	n.d. <sup>[d]</sup>	n.d.	n.d.	n.d.	n.d.
2a		6.6 (5.6–8.0)	9.1 (7.3–11)	33 (23–48)	43 (26–124)	47 (30–118)	> 500
2b		68 (57–80)	n.d.	31 (26–147)	n.d.	n.d.	> 500
2c		109 (87–137)	n.d.	n.d.	n.d.	n.d.	n.d.

[a] Dose response curves are shown in Figure S2. [b] Ref. [53]. [c] 95 % confidence interval. [d] n.d. = not determined, the compound was binding but EC<sub>50</sub> values could not be determined due to incomplete data.

pounds' binding to OPNA-AChEs and apo AChE suggest that the presence of OPNA or structural changes in AChE resulting from its covalent inhibition prevent the formation of key interactions between AChE residues and the compounds.

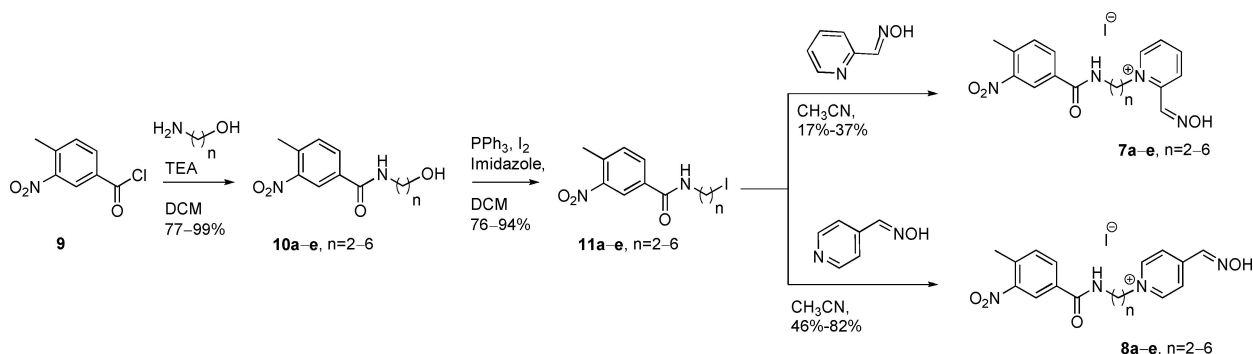
To verify the broad-spectrum binding of the aromatic scaffolds to the OPNA-AChE complexes, we examined three additional compounds (**1d–f**, Table S1)<sup>[59]</sup> containing the 4-methyl-3-nitrobenzamide scaffold but with different linkers and catalytic site-binding fragments. Encouragingly, these compounds exhibited similar broad-spectrum binding profiles to **1a** (Table S1 and Figure S2). We also investigated the binding pose of the 4-methyl-3-nitrobenzamide scaffold by determining the X-ray crystal structure of the complex between **1a** and *Mus musculus* AChE (*mAChE*) at a resolution of 2.3 Å (Table S2). *hAChE* and *mAChE* are very similar in sequence and 3D structure, and studies have shown similar inhibition kinetics.<sup>[66,67]</sup> Also, binary OPNA-AChE complex structures determined in both species are similar.<sup>[12,13,15,16]</sup> The molecular structure confirmed that the aromatic scaffold of **1a** interacts with amino acid residues at the entrance of the gorge, with the amine substituent extending towards the catalytic site (Figures 2B and S3). The aromatic moiety forms arene-arene stacking interactions with Tyr124 and Trp286, like the antidote HI-6. Importantly, the indole of Trp286 adopts a conformation differing from that seen in the apo structure, enabling the observed sandwich-type stacking interaction. In addition, there is a potential hydrogen bonding interaction between the nitro group of the 4-methyl-3-nitrobenzamide fragment and the backbone amide of Ser298 similar to that seen for HI-6. In summary, the 4-methyl-3-nitrobenzamide scaffold used in five different AChE inhibitors exhibited broad-spectrum binding to

three OPNA-AChE species, and binds to apo *mAChE* in a pose resembling that of the known reactivator HI-6. Our results also show that the TCSPC assay offer new possibilities to discover scaffolds that bind to OPNA-AChE. However, the long duration of the measurements as well as artefacts notable at high ligand concentrations limit the utility and throughput of the assay in its present form.

### Synthesis of reactivators

With the promising binding profiles of the 4-methyl-3-nitrobenzamide scaffold in hand, we proceeded to develop potential reactivators. The 4-methyl-3-nitrobenzamide scaffold was systematically combined with alkyl linkers of different lengths ( $n = 2–6$ ) to determine how the length of the linker between the aromatic scaffold and the oxime affects the reactivation of OPNA-inhibited AChE. For the reactive oxime moiety, we used the commonly used *ortho* and *para* pyridinium oxime moieties found in the clinically important reactivators HI-6 and obidoxime. This design strategy generated a set of 10 potential reactivators (**7a–e** and **8a–e**). A general synthetic route toward these molecules is presented in Scheme 1. Alcohols **10a–e** were obtained through amide coupling of acid chloride **9** with the corresponding amino alcohol, and the hydroxyl group was subsequently converted into an iodide under Appel conditions<sup>[68]</sup> to obtain alkyl iodides **11a–e**. These compounds were then heated by microwave irradiation with pyridine-4-aldoxime or heated to reflux with pyridine-2-aldoxime to provide the desired pyridinium oximes **7a–e** and **8a–e**.<sup>[69]</sup> Details of the synthetic procedures and analytical data for the





Scheme 1. General synthetic scheme describing the synthesis of *ortho* pyridinium oximes **7a–e** and *para* pyridinium oximes **8a–e**.

products and synthetic intermediates are available in the Supporting Information.

### Activity profiling of reactivators

To obtain an overview of the oximes' reactivation properties and guide subsequent in-depth biochemical and structural studies, we profiled the new compounds' reactivation capabilities. Using the activity-based Ellman assay,<sup>[70]</sup> we found that the  $IC_{50}$  values for the binding of compounds **7a–e** and **8a–e** to apo AChE were between 0.55  $\mu$ M and 25  $\mu$ M (corresponding to  $pIC_{50}$  values of 6.81 and 4.60, respectively; Figure 3); for comparative purposes, the  $IC_{50}$  value of the parent compound **1a** was 12  $\mu$ M ( $pIC_{50}$  4.92). The *ortho* pyridinium oximes **7a–e** displayed a SAR related to the length of the alkyl linker: a linker of four to six carbon atoms gave the strongest inhibition. Interestingly, the  $IC_{50}$  values for the *para* pyridinium oximes **8a–e** showed less variation than those for the *ortho* oximes, with no clear SAR, suggesting that the *ortho* and *para* molecules form at least partially different interactions with AChE. In the 2.5 Å crystal structure of the complex of mAChE with the *ortho* pyridinium oxime **7d**, which has a five-carbon linker (Table S3), the pyridinium moiety forms a T-shaped arene-arene interaction

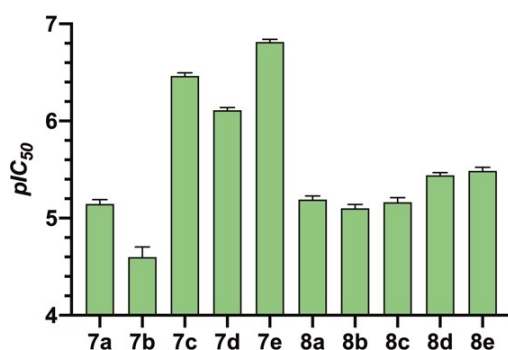


Figure 3. The  $pIC_{50}$  values for the binding of *ortho* oximes **7a–e** and *para* oximes **8a–e** to apo hAChE obtained by the Ellman assay. The alkyl linkers of the oximes ranges from two to six carbon atoms corresponding to letters a to e.

with the indole of Trp86 and the oxime substituent is accommodated in the oxyanion hole, potentially forming hydrogen bonds to Ser203O $\gamma$ , Gly121N, Gly122N, or Ala204N (Figures 4 and S4). This interaction pattern would be less favourable for compounds with shorter linkers and impossible for *para*-substituted oximes, clarifying the SAR for these compounds. The 4-methyl-3-nitrobenzamide moiety of **7d** forms an arene-arene sandwich with Tyr124 and Trp286 similar to that seen for **1a**.

AChE from human red blood cells was phosphorylated by tabun, sarin, cyclosarin, VX, or RVX to give the OPNA-AChE species tabun-AChE, sarin-AChE, cyclosarin-AChE, VX-AChE, and RVX-AChE. The oximes were subsequently screened for their efficiency in reactivating these OPNA-AChEs at concentrations of 1, 10, and 50  $\mu$ M (Table S4 and Figure S5). All of the oximes successfully reactivated all of the OPNA-AChE adducts, but their reactivation rates ( $k_{obs}$ ) were low, ranging from 0.0057 to 0.017  $min^{-1}$  at an oxime concentration of 10  $\mu$ M, depending on the oxime and OPNA species. Analysis of the reactivation profiles revealed a clear SAR of the tested compounds towards tabun-AChE and RVX-AChE (Figure 5), whereas all oximes

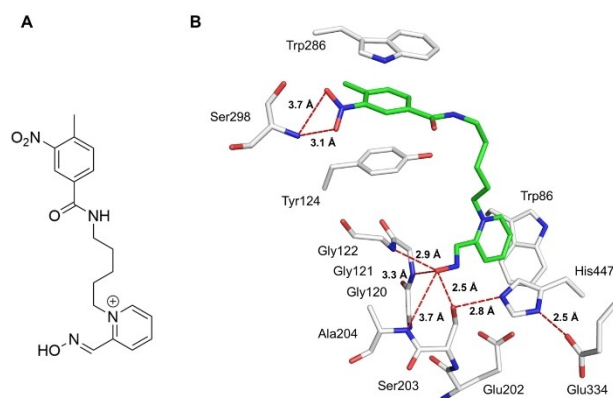
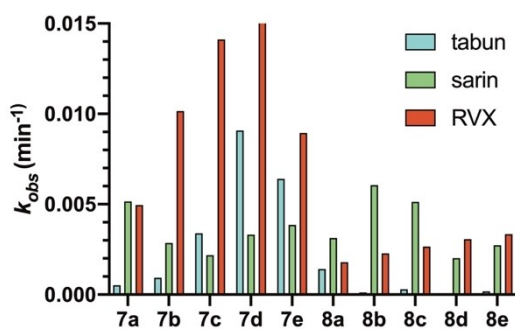


Figure 4. A) Chemical structure of reactivator **7d**. B) The crystal structure of a complex between **7d** (green) and mAChE (grey, pdb entry code 7QYN). Nitrogen and oxygen atoms are shown in blue and red, respectively, and potential hydrogen bonds are shown with dashed lines and their heteroatom distances.



**Figure 5.** Ortho oximes **7a–e** and para oximes **8a–e** efficiency in reactivating hAChE inhibited by the OPNAs tabun, sarin, and RVX at fixed oxime concentrations of 10  $\mu$ M. The alkyl linkers of the oximes ranges from two to six carbon atoms corresponding to letters a to e. Additional data is shown in Table S4 and Figure S5.

exhibited similar efficacy towards sarin-AChE, cyclosarin-AChE and VX-AChE. The *ortho* pyridinium oximes were considerably more efficient reactivators than the *para*-substituted ones (Table S4 and Figure S5). Spectrophotometric titration revealed that the *ortho* pyridinium oximes ( $pK_a=7.8–7.9$ ) were more prone to deprotonation than the *para* oximes ( $pK_a=8.1–8.4$ ) which may partly explain their reactivation SARs (Table S5). In accordance with the  $IC_{50}$  values determined for apo AChE, the SAR revealed that linkers with four to six carbon atoms gave higher reactivation rates, while shorter linkers were weaker reactivators. The most efficient overall reactivator, particularly for tabun and RVX, was the *ortho* pyridinium oxime **7d** with a five-carbon atom linker.

### Reactivation kinetics of **7d**

To better understand the kinetics of reactivation, experiments were performed to determine the dissociation constants ( $K_D$ ) and rates of displacement ( $k_r$ ) for complexes of **7d** with various OPNA-AChE adducts, enabling calculation of the corresponding second order rate constants ( $k_{r2}$ ) (Table 2 and Figure S6). In contrast to the activity profiling, which was performed using three reactivator concentrations and AChE from human red blood cells, the reactivation kinetics assays were performed at six to eight reactivator concentrations using recombinant human AChE.<sup>[71]</sup> Obidoxime was selected over HI-6 as the

reference reactivator in the experiments due to its ability to also reactivate tabun-inhibited AChE (HI-6 lack ability to reactivate tabun). These experiments revealed that **7d** had similar  $K_D$  values for all investigated OPNA-hAChEs, ranging from 25  $\mu$ M to 56  $\mu$ M. The affinity of **7d** for the inhibited enzymes was thus not greatly affected by the identity of the OPNA bound to Ser203 (Table 2). A similar, low variation of the  $K_D$  values have previously been reported for for example the oxime Ortho-7.<sup>[72]</sup> Conversely, the  $K_D$  values for obidoxime with OPNA-AChEs vary by as much as a factor of 35 depending on the bound OPNA.<sup>[4]</sup> The first-order displacement rate constants  $k_r$  varied by a factor of 5 across the five studied AChE species, ranging from 0.0093  $\text{min}^{-1}$  to 0.045  $\text{min}^{-1}$ ; RVX was displaced most rapidly and VX least rapidly. Obidoxime has substantially higher rate constants than **7d** for the displacement of all OPNA adducts other than that of tabun but also exhibits greater variation between OPNAs.<sup>[4]</sup> The second order rate constants ( $k_{r2}$ ) for **7d**, which depend on both  $K_D$  and  $k_r$ , revealed differences in the displacement of the OPNA adducts: the displacement of RVX was the most efficient ( $k_{r2} = 1.81 \text{ mM}^{-1} \text{ min}^{-1}$ ), followed by that of tabun ( $0.60 \text{ mM}^{-1} \text{ min}^{-1}$ ), while sarin was displaced with the lowest efficiency ( $0.19 \text{ mM}^{-1} \text{ min}^{-1}$ ). Notably, the  $k_{r2}$  values show that reactivation of tabun-AChE by **7d** was tenfold more efficient than by obidoxime. To summarize, the  $K_D$  and  $k_r$  reactivation constants of **7d** for different OPNAs varied by factors of two to five and were thus significantly less OPNA-dependent than those of obidoxime. These results show that the broad-spectrum binding profile of the 4-methyl-3-nitrobenzamide scaffold observed in the propidium iodide displacement assay is retained by the oximes and may also be reflected in the low variation of their  $K_D$  and  $k_r$  reactivation constants.

### Determination of target residence time

To complement the reactivation kinetics experiments, we investigated the initial reversible binding of **7d** to OPNA-AChE and the residence time of the resulting non-covalent complexes by studying the pre-steady state kinetics of their formation. To this end, stopped flow experiments with time resolutions of 5–1000 ms were performed to measure the quenching of the intrinsic protein fluorescence when **7d** was rapidly mixed with apo AChE or OPNA-AChEs. The systems' pre-activation kinetics could be studied because the time-scale of reactivation

**Table 2.** Dissociation constants ( $K_D$ ), reaction rate constants ( $k_r$ ), and second order rate constants ( $k_{r2}$ ) for **7d** and obidoxime, for reactivation of hAChE phosphorylated by five different nerve agents.

OPNA-hAChE	$K_D$ [ $\mu$ M] <b>7d</b>	obidoxime	$k_r$ [ $\text{min}^{-1}$ ] <b>7d</b>	obidoxime	$k_{r2}$ [ $\text{mM}^{-1} \text{ min}^{-1}$ ] <b>7d</b>	obidoxime
VX	$26.4 \pm 9.81$	– <sup>[a]</sup>	$0.00929 \pm 0.0009$	–	0.35	–
sarin	$56.0 \pm 7.82$	–	$0.0105 \pm 0.0004$	–	0.19	–
RVX	$24.7 \pm 5.85$	$611 \pm 154$	$0.0447 \pm 0.0030$	$0.443 \pm 0.0506$	1.81	0.73
cyclosarin	$54.0 \pm 6.49$	$738 \pm 156$	$0.0146 \pm 0.0006$	$0.163 \pm 0.0123$	0.27	0.22
tabun	$27.1 \pm 6.34$	$225 \pm 87.6$	$0.0164 \pm 0.0011$	$0.0152 \pm 0.00202$	0.60	0.060

[a] Not determined, the reactivation was too fast for the discontinuous assay used for the measurements.

was much slower than that of complex formation: the shortest reactivation half-life ( $t_{1/2}$ ) observed with **7d** was ~16 min for the reactivation of RVX-AChE. Binding of **7d** to apo AChE quenched the tryptophan fluorescence intensity in a concentration- and time-dependent manner, giving a residual fluorescence intensity of approximately 55 % at a **7d** concentration of 0.60  $\mu\text{M}$  (Figure 6A). The X-ray crystal structure of **7d** in complex with mAChE shows that **7d** forms contacts with Trp286 at the peripheral site and Trp86 in the catalytic site, suggesting that the quenching was mainly caused by these interactions (Figure 4B). Kinetic constants for the binding of **7d** were obtained by performing non-linear regression of the fluorescence intensity data to determine  $k_{\text{obs}}$ . The values of  $k_{\text{on}}$  and  $k_{\text{off}}$  were then determined by linear regression of the  $k_{\text{obs}}$  values for different concentrations of **7d** (Figure 6B, Table 3): the slope of the regression line is equal to  $k_{\text{on}}$ , the y-intercept is equal to  $k_{\text{off}}$  and the target residence time ( $\tau$ ) is the reciprocal of  $k_{\text{off}}$  (Table 3). The  $k_{\text{on}}$ ,  $k_{\text{off}}$  and  $\tau$  for the binding of **7d** to apo AChE were  $7.83 \times 10^7 \text{ M}^{-1} \text{ s}^{-1}$ ,  $41.88 \text{ s}^{-1}$ , and 0.024 s, respectively, and the association constants of **7d** were on the same order of magnitude as those reported previously for charged oximes with a triazole motif.<sup>[36,64]</sup> For comparative purposes, the

turnover number ( $k_{\text{cat}}$ ) for acetylthiocholine hydrolysis under steady state conditions is much higher – approximately  $6500 \text{ s}^{-1}$ .<sup>[73]</sup> Studies on the pre-activation kinetics of **7d**'s binding to tabun-AChE showed that the level of quenching was lower than in the case of the apo enzyme; the residual fluorescence intensity at a **7d** concentration of 0.60  $\mu\text{M}$  was 83 % (Figures 7A and B). Furthermore, the association ( $k_{\text{on}}$ ) was noticeably slower and the measurements required a different time scale than for the apo enzyme (Table 3). We also observed a second binding phase at higher concentrations of **7d**, reducing the residual fluorescence intensity to ~40 % (Figures 7C–D). We propose that the initial phase (i.e., quenching to a residual fluorescence intensity of 83 %) was due to interactions between **7d** and Trp286 while the second phase (i.e., quenching to a residual fluorescence intensity of ~40 %) was due to interactions between **7d** and Trp86 at the bottom of the gorge.

A similar initial phase was observed when studying the pre-activation kinetics of **7d** binding to VX-AChE and RVX-AChE, with rapid quenching to a residual fluorescence intensity of approximately ~80 % followed by a second slower phase reaching a residual fluorescence intensity of ~50 %. In these

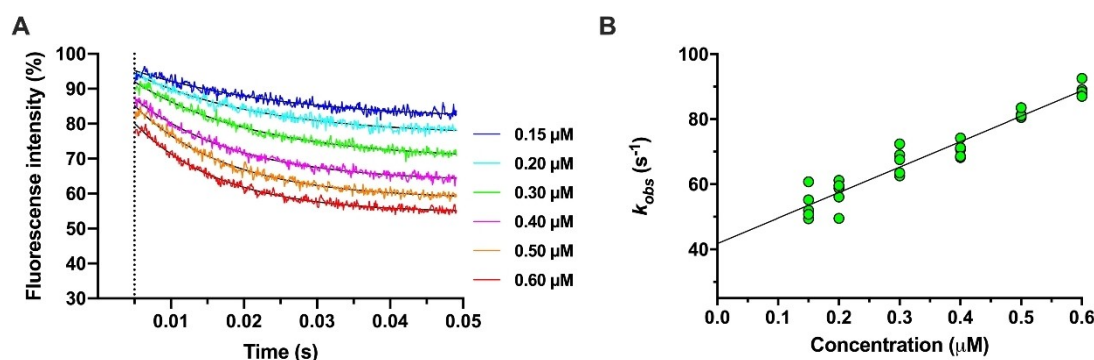


**Figure 6.** A) Pre-steady state kinetics of the binding of **7d** to apo hAChE studied by stopped flow measurements showing the time dependence of the intrinsic protein fluorescence quenching when **7d** is rapidly mixed with apo hAChE. The six tested concentrations of **7d** ranged from 0.15 to 0.60  $\mu\text{M}$ . The vertical dotted line represents the 5 ms dead-time of the instrument and the solid lines for each oxime concentration are non-linear regression using the equation for exponential decay. B) Secondary plot of the  $k_{\text{obs}}$  values from which the  $k_{\text{on}}$  and  $k_{\text{off}}$  values were determined (Table 3). All replicates are shown.

**Table 3.** Pre-equilibrium kinetics for the binding and unbinding of **7d** to apo hAChE and hAChE phosphorylated by five different nerve agents.

Initial phase Sample hAChE	$k_{\text{on}}$ [ $\text{M}^{-1} \text{s}^{-1}$ ]	$k_{\text{off}}$ [ $\text{s}^{-1}$ ]	$K_{\text{D}}$ [ $\mu\text{M}$ ]	$\tau$ [s]	$R^2$
apo	$7.83 \pm 0.40 \times 10^7$	$41.88 \pm 1.56$	0.53	0.024	0.93
tabun-	$1.45 \pm 0.14 \times 10^7$	$2.55 \pm 0.71$	0.18	0.39	0.81
sarin-	$23.30 \pm 0.29 \times 10^7$	$29.36 \pm 11.66$	0.13	0.034	0.69
cyclosarin-	n.d. <sup>[a]</sup>	n.d.	n.d.	n.d.	n.d.
VX-	n.d.	n.d.	n.d.	n.d.	n.d.
RVX-	n.d.	n.d.	n.d.	n.d.	n.d.
second phase					
apo	n.b. <sup>[b]</sup>	n.b.	n.b.	n.b.	n.b.
tabun-	$0.35 \pm 0.09 \times 10^7$	$3.71 \pm 0.87$	1.00	0.27	0.98
sarin-	n.b.	n.b.	n.b.	n.b.	n.b.
cyclosarin-	n.b.	n.b.	n.b.	n.b.	n.b.
VX-	$0.53 \pm 0.29 \times 10^7$	$4.99 \pm 2.15$	0.94	0.20	0.92
RVX-	$0.24 \pm 0.12 \times 10^7$	$2.33 \pm 1.19$	0.96	0.43	0.93

[a] n.d. = not determined, binding was observed by a rapid quenching of the fluorescence intensity but no  $k_{\text{obs}}$  values could not be determined due to incomplete data. [b] n.b. = no binding, binding was not observed with current experimental conditions (i.e. no quenching of the fluorescence intensity).



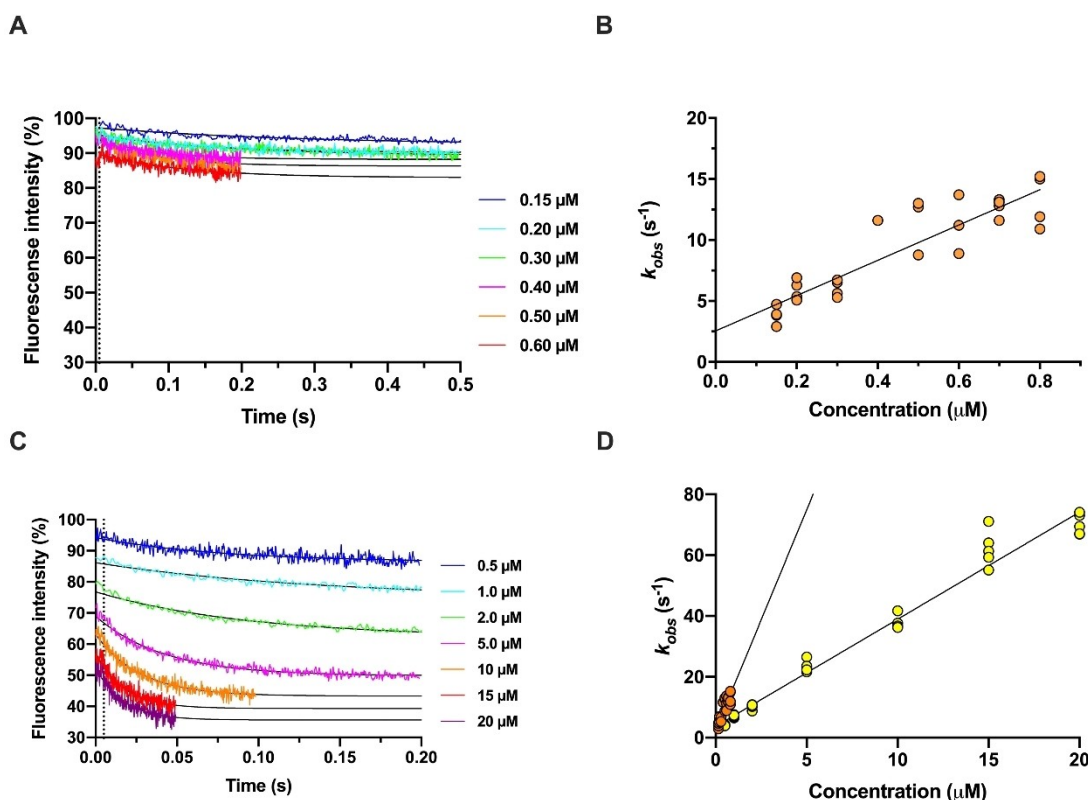


**Figure 7.** Pre-steady state kinetics of the binding of **7d** to tabun-*hAChE* studied by stopped flow measurements showing the time dependence of the intrinsic protein fluorescence quenching when **7d** is rapidly mixed with tabun-*hAChE*. A,C) The tested concentrations of **7d** ranged from 0.15 to 0.60  $\mu\text{M}$  (A) and 0.50 to 20  $\mu\text{M}$  (C). The vertical dotted line represents the 5 ms dead-time of the instrument and the solid lines for each oxime concentration are non-linear regression using the equation for exponential decay (the regressions lines for 0.4–0.6  $\mu\text{M}$  were extrapolated to 0.2 s for comparisons). B,D) secondary plots of the  $k_{\text{obs}}$  values from which the  $k_{\text{on}}$  and  $k_{\text{off}}$  values were determined (Table 3). All replicates are shown. As a reference, data from the lower concentrations (B) is also included in (C) in orange. The linear regression lines are shown in black.

cases, we could only generate reliable  $k_{\text{obs}}$  values and determine  $k_{\text{on}}$  and  $k_{\text{off}}$  of the second phase (Table 3, Figure S7). The pre-activation kinetics of **7d** binding to sarin-AChE and cyclo-sarin-AChE showed a different pattern with an initial rapid quenching to  $\sim 80\%$  fluorescence intensity but no secondary binding phase even at **7d** concentrations as high as 10  $\mu\text{M}$ .

In summary, the data revealed three different kinetic profiles: i) a rapid decline to 55% residual fluorescence intensity (apo), ii) a rapid decline to  $\sim 80\%$  residual intensity followed by a slower decline to  $\sim 40\text{--}50\%$  (tabun, VX and RVX), and iii) a rapid decline to  $\sim 80\%$  residual intensity with no detectable secondary phase at the time resolution of the instrument (sarin and cyclosarin). The constants describing the initial reversible binding of **7d** depend heavily on the AChE species being studied (Table 3). For example, both association and dissociation were slower for tabun-AChE than for apo AChE. Conversely, the association of **7d** to sarin-AChE was faster than that to apo AChE. This indicates that the formation of the OPNA-AChE serine phosphoester at the bottom of the gorge influenced the pre-activation kinetics at the peripheral site via an allosteric mechanism. Furthermore, the kinetic constants for the association and dissociation of **7d** with tabun-AChE differed by more than an order of magnitude from those for sarin-AChE, suggesting that the identity of the OPNA affects the initial

binding of **7d**. The second binding phase involved quenching of both Trp286 and Trp86 and was only observed during the binding of **7d** to tabun-, VX- and RVX-AChE. A comparison of the pre-steady state kinetic constants to those obtained under steady state conditions (on the time-scale of reactivation) revealed a positive correlation between the residence time of **7d** ( $\tau$ ) and the reactivation rate constants  $k_r$  and  $k_{r2}$  for tabun-, VX- and RVX-AChE, suggesting that the target residence time is an important parameter for reactivator design and discovery. Furthermore, the absence of a secondary binding phase for **7d** with sarin- and cyclosarin-AChE together with the finding that the residual fluorescence intensity was around 80% for these enzyme adducts when maximally quenched by **7d** indicates that **7d** mainly interacts with Trp286 at the peripheral site but not with Trp86 at the catalytic site, in accordance with its low reactivation efficacy.

### Structures of **7d** in complex with OPNA-inhibited AChE

Reactivators are also active in crystalline complexes of *mAChE* inhibited by an OPNA, and we have recently shown that their pre-activation conformations can be trapped using a combination of crystallographic and computational approaches.<sup>[58]</sup>

Therefore, to obtain structural insights into the reactivation process, we inhibited crystals of *m*AChE with VX, sarin, RVX, or tabun (Table S6).

After complete inhibition, the OPNA-*m*AChE crystals were soaked with **7d** to enable investigation of potential differences in binding poses that could be relevant to the rate and overall efficacy of reactivation. X-ray data were collected after a short incubation and vitrification of the crystals to arrest the reactivation. The final structures exhibit almost full occupancy (>0.9) of both the OPNA adducts and **7d**, showing that pre-activation conformational states were successfully trapped (Table S7). The electron density maps of the aromatic scaffold are clearly defined. However, as in previous studies on reactivators on OPNA-*m*AChE, the electron density maps of the pyridinium oximes and linkers are weak and partly disordered, regardless of the OPNA bound to the catalytic site. The electron density defining **7d** in complex with VX-*m*AChE enabled complete modelling of the reactivator, but the corresponding densities for **7d** in complexes with tabun-, RVX- or sarin-*m*AChE could only partly be modelled using conventional crystallographic approaches.

While differences in crystal packing and experimental conditions makes direct comparisons difficult, crystal structures of HI-6•OPNA-*h*AChE show that this system appears to have a lower degree of flexibility than corresponding complexes with *m*AChE.<sup>[12,13]</sup> The main differences are that in the OPNA-*h*AChE complexes the electron density maps clearly defined the entire HI-6 ligand,<sup>[12,13]</sup> while in OPNA-*m*AChE the linkers and pyridinium oximes can be partly disordered depending on the inhibiting OPNA and reactivator. Interestingly, the aromatic scaffolds of the reactivators appears to be clearly defined in both *h*AChE and *m*AChE and, for example, the conformational change of Trp286 is observed in both. In this study, we have found that the kinetics and SAR obtained using *h*AChE can be analysed and rationalized using crystal structures of *m*AChE as discussed in the following sections, but we also note that the interpretation of data should be made with some caution due to potential species differences.

The structural analyses revealed three distinct binding modes of the 4-methyl-3-nitrobenzamide scaffold of **7d**, depending on the OPNA inhibiting *m*AChE. In ternary complexes of *m*AChE inhibited by tabun and RVX, **7d** forms an arene-arene sandwich with Tyr124 and Trp286 (mode A), analogous to the structures of **1a** and **7d** complexed with free *m*AChE (Figures 8A and B, S8 and S9). For *m*AChE inhibited by VX, the aromatic scaffold of **7d** forms a parallel displaced arene-arene interaction with the indole of Trp286 and there is a potential hydrogen bond between the nitro group of **7d** and Phe295N (mode B, Figures 8C and S10). For *m*AChE inhibited by sarin, the 4-methyl-3-nitrobenzamide scaffold forms an arene-arene interaction similar to that in mode B, but the entire reactivator ligand has a different binding pose in which the pyridinium oxime projects out from the binding gorge and is exposed to the bulk solvent (mode C, Figures 8D and S11). These findings show that the 4-methyl-3-nitrobenzamide scaffold can bind to the entrance of the gorge in a variety of ways in different OPNA-*m*AChE complexes. The electron density maps show that binding modes A and B of the aromatic scaffold position the pyridinium oxime in close proximity to the serine phosphoesters of tabun and RVX (mode A) and VX (mode B) whereas in mode C the oxime is far from the catalytic site inhibited by sarin. The promiscuity of the peripheral site of OPNA-*h*AChE in accommodating aromatic scaffolds has also been observed for HI-6.<sup>[12,13]</sup> In this case different arene-arene interactions lead to different binding poses for the aromatic scaffold of HI-6, while the linker and pyridinium oxime are directed towards the active site for all HI-6-OPNA-*h*AChE species.

Reactivation by nucleophilic attack on the phosphorus of the Ser203-OPNA adduct is only possible if the phosphorus is sterically accessible. Inspection of crystal structures shows that the O-alkyl moieties of some OPNA adducts shield the phosphorus,<sup>[15,74]</sup> preventing the adoption of a spatial orientation favouring nucleophilic attack.<sup>[58]</sup> In the ternary complex of **7d** with tabun-*m*AChE, the O-alkyl moiety of the tabun phosphoester adopts an open conformation not seen in the

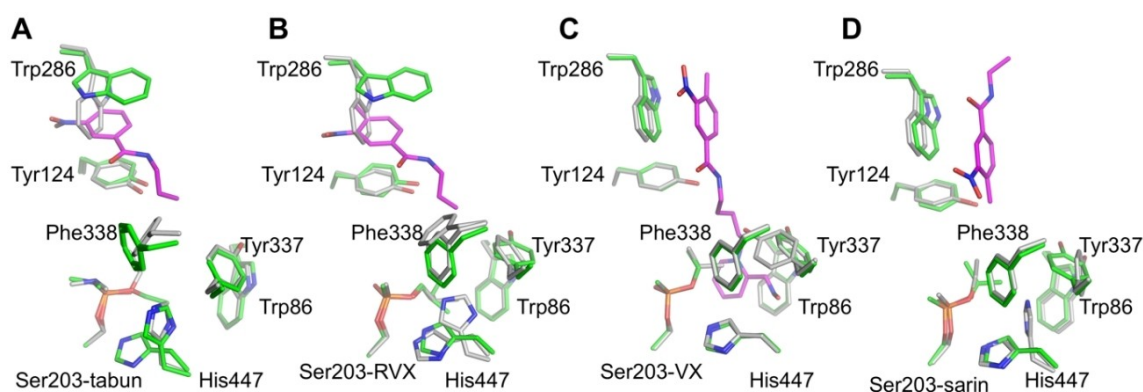


**Figure 8.** Crystal structures show three observed binding modes for **7d** (magenta) in complex with OPNA-*m*AChE (green), including the resulting ligand-induced changes as seen when superimposed onto the binary OPNA-*m*AChE complex (in white). Binding mode A is observed for **7d** in complex with tabun-*m*AChE (A), and RVX-*m*AChE (B). Binding mode B is observed for **7d** in complex with VX-*m*AChE (C), and binding mode C for **7d** in complex with sarin-*m*AChE (D). Oxygen, nitrogen, and phosphorus are displayed in red, blue, and orange, respectively. The figure was generated by using the pdb entry codes 7R2F, 7R4E, 7R3C, 7R0A, 3DL4, 2Y2V, 2Y2U and 3ZLT.

binary complex of tabun-*m*AChE.<sup>[15]</sup> The O-alkyl moiety of the RVX adduct also adopts an open conformation in the ternary complex of **7d** in line with the previously reported RVX-*m*AChE complex,<sup>[16]</sup> and may be partly responsible for its higher reactivation rate when compared to the sarin and VX adducts. The O-alkyl moiety of VX-AChE was modelled in a closed conformation in both the previously reported binary complex<sup>[74]</sup> and the ternary **7d**-VX-AChE complex. However, careful inspection of the electron density maps revealed that an alternative low occupancy open conformation could be possible in our ternary complex. Binding mode B of **7d** in the ternary complex with VX-AChE appears to be non-productive for reactivation because an arene-arene interaction between the pyridinium oxime and Trp86 causes the nucleophilic oxime to be positioned far from the adduct's phosphorus atom. A similar non-productive binding mode was observed in the ternary complex of HI-6 with a sarin-AChE adduct,<sup>[58]</sup> in which the O-alkyl chain of the OPNA adduct projects towards the entrance of the gorge in the closed conformation. Such a conformation is also seen in binary complexes of sarin-*m*AChE.<sup>[58]</sup> These results suggest that steric hindrance imposed by the O-alkyl chain of sarin prevents the pyridinium oxime moiety from entering the catalytic site, forcing the adoption of the non-productive binding mode C. However, because the kinetic data indicate that both VX-*h*AChE (mode B) and sarin-*h*AChE (mode C) are susceptible to reactivation, we propose that reactivation of these complexes proceeds via binding mode A or some other productive binding mode that has yet to be characterized. We hypothesise that the occupancy of the productive complexes of **7d**-VX-*h*AChE and **7d**-sarin-*m*AChE may be too low to be detected in the current crystallographic data.

In comparison to the binary OPNA complexes<sup>[15,16]</sup> (i.e. tabun-*m*AChE, sarin-*m*AChE, VX-*m*AChE and RVX-*m*AChE), the data for the ternary complexes show that the conformations of amino acid residues in proximity to the OPNA phosphoester are affected by the binding of **7d**. This is particularly evident for His447, but the side chains of Phe338 and Tyr337 also show minor structural adjustments. Because the occupancies of the OPNA adducts are high, we suggest that the binding poses of **7d** correspond to low energy conformations that precede the reactivation reaction (mode A) or alternative non-productive binding poses that cannot directly proceed to the pre-activation complex (modes B and C). In a recent study by Kovalevsky and co-workers,<sup>[14]</sup> room temperature X-ray structures of native and VX-phosphorylated *h*AChE with an imidazole-based oxime (RS-170B) show that inhibition by VX triggers substantial conformational changes in the bound reactivator. The authors propose that their observed non-productive binding poses of RS-170B may explain its poor reactivation abilities of VX-*h*AChE.

To summarise, our crystallographic studies show that there is an intricate structural interplay between the binary OPNA-AChE adducts and the reactivator **7d**, leading to ternary complexes with different structural prerequisites for productive reactivation.

## Computational modelling of **7d**-tabun-AChE

Tabun inhibits AChE by forming a covalent adduct that is resistant towards many clinically important oxime reactivators.<sup>[4]</sup> Interestingly, the reactivation kinetics data revealed that the efficacy ( $k_{r2}$ ) of **7d** against this adduct was ten times higher than that of obidoxime. To elucidate the structural basis for this outcome, we performed further structural analysis of the ternary complex of **7d** with tabun-AChE. We have previously combined X-ray crystallography with a quantum chemical cluster approach to refine and analyse chemically plausible binding modes of the antidote HI-6.<sup>[58]</sup> However, unlike in the case of HI-6, the electron density map of the pyridinium oxime of **7d** was consistent with multiple conformations. We therefore performed conformational sampling of the pyridinium oxime and linker using molecular mechanics, examining multiple tautomers and protonation states of His447 (Figure S11 and Table S8). This revealed that the linker and pyridinium oxime of **7d** are highly mobile despite being anchored by the aromatic ring at the entrance of the gorge. Three populations of conformers were obtained, one where the oxime pointed towards His447, a second where the nucleophilic oxime was directed towards the tabun phosphoester, and a third presumably unproductive conformation where the pyridinium oxime was directed away from both the tabun phosphoester and His447. To verify the chemical relevance of the different potential pre-activation conformations, three conformational states from the first two populations were subjected to geometry optimization using density functional theory (DFT). The results revealed three chemically stable systems representing potential pre-activation conformations. In the first conformer (C1), the reactivator oxime is protonated and projects towards the non-protonated nitrogen of His447 (OH...N distance = 1.9 Å; Figure 9A). In the second conformer (C2), the oxime is deprotonated and the nitrogen of His447 is protonated (O...HN distance = 1.8 Å; Figure 9B). These two conformers represent potential pre-activation states where the oxime of **7d** is transformed into a stronger nucleophile in situ by His447, a mechanism also proposed for other oximes. In the third conformer (C3), the deprotonated oxime is displaced by 5 Å compared to C1 and C2 and adopts a pre-activation pose in which it is 4.6 Å away from the tabun phosphorus centre, potentially preceding a nucleophilic attack (Figure 9C). Superposition of the structure of C3 onto the crystal structure of the pre-activation complex of HI-6 binding to sarin-AChE<sup>[58]</sup> shows that the oximes occupy similar positions, although HI-6's oxime is closer to the phosphorus. In summary, computational modelling revealed three chemically stable pre-activation states that may explain **7d**'s highly efficient reactivation of tabun-AChE and could be used to guide further reactivator optimization.

## Discussion

The 4-methyl-3-nitrobenzamide fragment was identified as a potential broad-spectrum reactivator scaffold by studying the

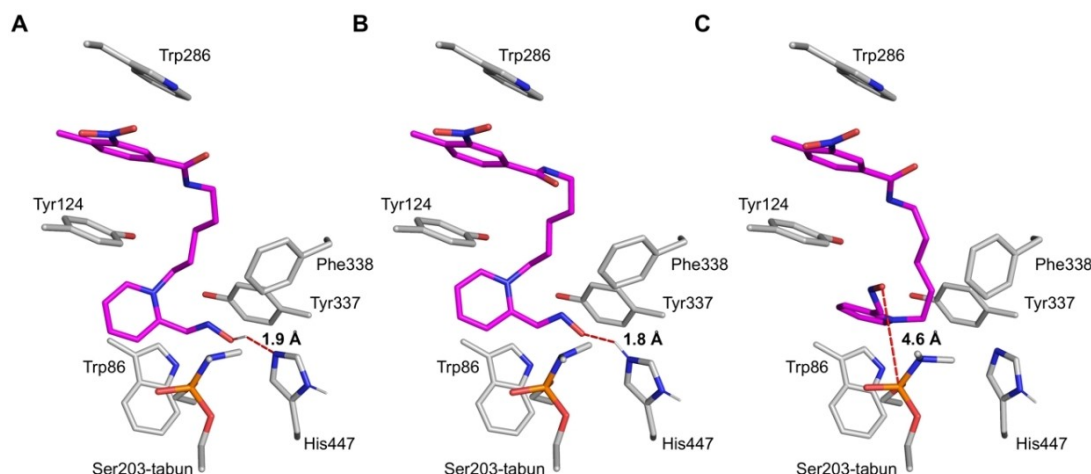


**Figure 9.** The three modelled conformations of **7d** (magenta) in complex with tabun-*mAChE* (grey), determined from a conformational search and subsequent geometry optimization. A) The protonated oxime is positioned towards neutral His447. B) The deprotonated oxime is positioned towards protonated His447. C) The deprotonated oxime is positioned towards the tabun-serine adduct. Oxygen, nitrogen, hydrogen, and phosphorus are displayed in red, blue, white, and orange, respectively. The distances between the oximes and His447 or OPNA adduct, respectively, are marked with dotted lines.

binding of a set of non-reactive molecules to OPNA-AChE species. Accordingly, a set of oximes incorporating this fragment exhibited reactivation performance and one, **7d**, successfully reactivated all studied OPNA-inhibited AChE adducts. Moreover, the reactivation performance of **7d** was less sensitive to the identity of the OPNA than that of the established drug obidoxime. This property has also been observed in other newly developed reactivators, for example, the tacrine-linked reactivators designed and synthesised by Nachon and coworkers.<sup>[45]</sup> By supplementing knowledge of steady-state reactivation kinetics with data on pre-equilibrium (pre-activation) kinetics and X-ray crystallography, we discovered that this scaffold functions in an unexpectedly complex way. Specifically, it was found that the 4-methyl-3-nitrobenzamide moiety of **7d** can adopt different binding poses in different OPNA-AChE species and that its binding involves multiple interactions formed on different time scales. The strong quenching of the tryptophan fluorescence intensity in the pre-activation experiments suggests that **7d** interacts with both the peripheral site (i.e. Trp286) and the lower part of the binding gorge (i.e. Trp86) of tabun-AChE, RVX-AChE and VX-AChE. The crystal structures of the ternary complexes confirmed that the linker and pyridinium oxime of **7d** are oriented towards the tabun, RVX and VX phosphoesters located in the vicinity of Trp86. Interestingly, the results for **7d** in complex with sarin-AChE were different: in this case, the degree of tryptophan quenching was lower and it occurred on a shorter time scale, indicating that the dominant **7d** population interacted only with the peripheral site. Accordingly, in the crystal structure of this complex, the linker and pyridinium oxime are oriented towards the solvent and do not interact with Trp86. Notably, Trp286 adopts a “flipped” conformation in the complexes of **7d** with tabun-AChE and RVX-AChE but retains an apo-like conformation in complexes of **7d** with VX-AChE and sarin-AChE. The 4-methyl-3-nitrobenzamide scaffold thus has at least three clearly distinguishable inter-

action patterns with OPNA-AChE species that form on different timescales and have different population sizes in the conformational landscapes of **7d**-OPNA-AChE complexes. The design of nerve agent reactivators has historically been guided by data representing steady-state experimental conditions including IC<sub>50</sub> values and reactivation kinetics parameters as well as most of the deposited X-ray crystal structures of AChE in complex with nerve agents or reactivators. However, the results presented herein show that **7d** displays highly variable pre-activation binding kinetics and binding geometries. This diversity in binding is apparent even during the early binding events when **7d** approaches Trp286, a residue located at the entrance of the gorge, far from the OPNA moiety within the OPNA-AChE adduct. Our results thus show that inhibition by OPNAs changes the conformational landscape and dynamics of AChE such that distant early binding events are affected allosterically.

The displacement rates ( $k_p$ ) of the methylphosphonate adducts sarin-AChE, VX-AChE and RVX-AChE show that the reactivation reaction of the latter was more than four times faster than those of the other two. This is due to the different O-alkyl moieties of the OPNA-adducts: the isobutoxy group of RVX-AChE is more sterically demanding than the isopropoxy group of sarin-AChE and the ethoxy group of VX-AChE (Figure 1). The cleavage of the serine phosphoester has been proposed to proceed via a pentavalent intermediate, conceptually similar to a carbonyl addition, based on computational studies<sup>[75,76]</sup> and the conformation of the O-alkyl moiety will influence the transition state energy and the accessibility of the phosphorus. It should be noted, however, that many computational studies focus either in the formation of the pre-activation complex and binding of a peripheral site ligand, or on the details of the reactivation mechanism, yet rarely both.<sup>[77,78]</sup> We previously hypothesised that the reactivation of sarin-AChE by HI-6 depends on a conformational change of the

O-alkyl moiety of sarin and its interaction with Glu202.<sup>[58]</sup> Here we have shown that RVX-AChE, which has an open O-alkyl conformation, reacts more rapidly than sarin-AChE and VX-AChE, which have closed conformations. Tabun-inhibited AChE is known to be inherently difficult to reactivate because its serine phosphoester is a dimethylphosphoramidate instead of a methylphosphonate.<sup>[15]</sup> Despite this, our reactivation data show that tabun-AChE has a higher displacement rate than VX-AChE and sarin-AChE. Interestingly, the adduct of tabun-AChE also has an ethoxy group like VX-AChE. However, the ethoxy group of tabun-AChE has an open conformation in the ternary complex whereas that of VX-AChE has a closed conformation. Furthermore, our computational studies showed that **7d** can adopt multiple chemically stable conformations in the binding site of tabun-AChE that facilitate deprotonation of the oxime by His447, a transformation necessary for the reaction. It should be noted that although **7d** and obidoxime have similar displacement rates ( $k_t$ ), **7d** has a 10-fold lower dissociation constant ( $K_D$ ), explaining its efficient reactivation of tabun-AChE. We also note a positive correlation between the residence time of **7d** and its reactivation efficacy. Although the experimental data presented here are limited and more studies are needed, this observation supports our hypothesis that a sufficiently long  $\tau$  is required for the binding of the reactivator in a position that allows subsequent displacement of the phosphorus adduct.

## Conclusions

To enable the rational design of new and efficient reactivators of AChE following OPNA intoxication, the complexity of the AChE/OPNA/reactivator system must be dissected by using approaches and tools that support iterative design and evaluation processes. This work presents such an approach in which the identification of a broad-spectrum fragment binding to the peripheral site of AChE was followed by the synthesis of candidate pyridinium oximes incorporating this fragment. Activity profiling of these oximes was then performed to identify optimal linker lengths, leading to the discovery of the broad-spectrum reactivator **7d**. The reactivation properties of **7d** were analysed in detail by studying its reactivation and pre-activation kinetics, which were linked to structural data obtained through X-ray crystallography and computational chemistry. This revealed that efficient reactivation by **7d** was linked to longer residence times and strong quenching of the tryptophan fluorescence intensities in the pre-activation phase, indicating that early non-covalent interactions must be considered during reactivator discovery. Furthermore, the X-ray crystal structures showed that in the ternary complexes with the highest displacement rates, **7d** binds with the pyridinium oxime oriented towards the OPNA serine phosphoester and the O-alkyl chain in an open conformation, making the phosphorus accessible for nucleophilic attack. Importantly, **7d** was shown to reactivate tabun-AChE ten times more rapidly than obidoxime (HI-6 cannot reactivate this adduct at all). A computational study of **7d**-tabun-AChE revealed the existence of pre-activation conformational states that may be linked to the low  $K_D$  and

efficient reactivation of this complex. These findings could be used to guide structure-based design efforts to improve reactivation efficiency.

In conclusion, this study has shown that new strategies and methods enable a rational and iterative discovery process that could facilitate the discovery of clinically useful broad-spectrum AChE reactivators.

## Experimental Section

**Expression and purification of hAChE:** Wild type hAChE was expressed as previously described.<sup>[71]</sup> The material used for the TCSPC binding assay was prepared and purified using procaine amide coupled Sepharose as previously reported.<sup>[79]</sup>

We found that storing the protein samples at a concentration of a 3–5 mg/mL increased the stability and recovery of the protein. The concentrated enzyme was divided into small aliquots, frozen in liquid nitrogen, and stored at  $-80^\circ\text{C}$  until use in  $\text{IC}_{50}$  or TCSPC displacement assays, or reactivation kinetics experiments.

**Assessment of ligand binding to selected OPNA-AChEs:** To investigate the binding of non-reactive ligands to AChE inhibited by various OPNAs, we measured the competitive displacement of the fluorescent probe propidium iodide in a previously reported biophysical assay.<sup>[16]</sup> The design, synthesis,  $\text{IC}_{50}$  values, and QSAR analysis of the investigated compounds was reported previously.<sup>[59]</sup> In brief, binding data were obtained by measuring the fraction of free (i.e. solution-phase) and hAChE-bound propidium iodide at different ligand concentrations. First, OPNA-inhibited AChE was generated by incubating purified hAChE with 5 mM of VX, RVX, tabun or DFP. After an incubation of 5–15 min, complete inhibition was verified by enzyme activity measurements using the Ellmann assay. Once the inhibition reached at least 99%, the excess inhibitor was removed using a NAP-5 column (GE-healthcare) and the inhibited protein was immediately frozen. Control samples were treated in the same manner except that the OPNA was substituted with buffer. The final concentration of hAChE in the assays was approximately 1.0–1.5  $\mu\text{M}$ . The competitive displacement experiments were performed by mixing the protein with 2.25  $\mu\text{M}$  propidium iodide in an assay buffer consisting of 10 mM Tris-HCl and 50 mM NaCl, pH 8.0. Stock solution of the inhibitors were first prepared in DMSO at a concentration of 100 mM. Further dilutions were done in the assay buffer. The inhibitors were added stepwise to the cuvettes to increase their concentrations. At each step (i.e., each inhibitor concentration), the ratio of free to AChE-bound propidium iodide was measured using time-correlated single photon counting (TCSPC).<sup>[16]</sup> The binding of the inhibitors to apo hAChE, tabun-hAChE, VX-hAChE, RVX-hAChE, and DFP-AChE was studied (see Figure S2 for typical concentration intervals and binding curves). Binding curves were analysed by non-linear regression using GraphPad Prism version 8 for OSX (GraphPad Software, La Jolla, USA). The data in Figure 2 B was normalized using the normalize function with the largest value in the data set defined as 100% and the lowest value in the dataset defined as 0%.

**Expression, purification, crystallization and refinement of mAChE:** Wild-type AChE derived from *Mus Musculus* was expressed in HEK293F cells, and purified and crystallised as previously described.<sup>[79]</sup> In brief, HEK293F cells expressing secreted mAChE were grown in suspension using Freestyle 293 and Glutamax (Gibco) media containing 20  $\mu\text{g/mL}$  Gentamicin (Gibco). Before purification, the mAChE-containing supernatant was centrifuged and the cleared supernatant was purified using affinity and size



exclusion chromatography. Protein crystallization was done by the hanging drop vapor diffusion method, at a protein concentration of 10 mg/mL with a well solution containing 27–30% (w/v) PEG750MME and 0.1 M HEPES, pH 6.9–7.1. The binary (oxime-AChE) complexes and the ternary OPNA (oxime•OPNA-AChE) complexes were generated by soaking the inhibitors into mAChE crystals prior to flash freezing in liquid nitrogen as previously described.<sup>[54,57,79,80]</sup> X-ray data collection was carried out at the MAX-lab synchrotron (Lund, Sweden), on beamlines I911-2 and I911-3 equipped with MAR Research CCD detectors. The intensity data were indexed and integrated by XDS<sup>[81]</sup> and scaled using Scala.<sup>[82]</sup> The structures were determined by rigid-body refinement with a modified apo structure of mAChE (PDB entry code 1J06) as a starting model. Further crystallographic refinement and manual rebuilding were carried out using the Phenix software suite,<sup>[83]</sup> and COOT.<sup>[84]</sup> The quality of the models was validated using MolProbity (as implemented in the Phenix software suite) and the wwPDB Validation Service (<https://validate.rcsb-1.wwpdb.org/>). Data collection and refinement statistics are listed in Tables S2–S3 and S6. The coordinates and structure factors have been deposited in the RCSB Protein Data Bank with accession codes 7R02, 7QYN, 7R2F, 7R3C, 7R4E, and 7R0A for 1a-mAChE, 7d-mAChE, 7d-tabun-mAChE, 7d-VX-mAChE, 7d-RVX-mAChE and 7d-sarin-mAChE, respectively. Detailed descriptions of the structures are provided in the Supporting Information.

**General synthetic procedures:** Chemicals were purchased from Sigma-Aldrich Co. and used without further purification. Reactions were performed under an inert atmosphere using dried glassware and dry solvents. Solvents were dried using a PPT/Glass Contour Solvent Purification System (CH<sub>2</sub>Cl<sub>2</sub>) or 3 Å molecular sieves (CH<sub>3</sub>CN). Microwave heating was performed with a Biotage Initiator 400 W, TLC was performed on silica gel 60 F<sub>254</sub>, and column chromatography was performed with a Biotage SNAP cartridge KP-Sil attached to a Biotage Isolera system. Preparative reverse-phase HPLC was performed on a Gilson GX-271 instrument equipped with a Machery-Nagel C<sub>18</sub> HTEC Column (250×21.0 mm, 5 µm) with a gradient of H<sub>2</sub>O and CH<sub>3</sub>CN with 0.005% formic acid and a gradient of 10–60% CH<sub>3</sub>CN, flowrate 18 mL/min over 20 min, and detection at 214 nm. LC–MS analysis was performed on a Waters LC system equipped with an Xterra MS C18 column (4.6×50.0 mm, 18.5 µm), with a gradient of H<sub>2</sub>O and CH<sub>3</sub>CN with 0.2% formic acid, with detection at 214 and 254 nm. Mass spectra were obtained with a Waters micromass ZG 2000 instrument with positive and negative ionization. <sup>1</sup>H NMR and <sup>13</sup>C NMR spectra were recorded on a Bruker DRX-400 spectrometer at 298 K, in (CD<sub>3</sub>)<sub>2</sub>SO solution (residual (CH<sub>3</sub>)<sub>2</sub>SO δ<sub>H</sub> 2.50 ppm, δ<sub>C</sub> 39.52 ppm) or CDCl<sub>3</sub> solution (residual CHCl<sub>3</sub> δ<sub>H</sub> 7.26 ppm, δ<sub>C</sub> 77.16 ppm) or CD<sub>3</sub>OD solution (residual CH<sub>3</sub>OD δ<sub>H</sub> 3.31 ppm, δ<sub>C</sub> 49.0 ppm). Target compounds were ≥ 95% pure according to LC–MS UV traces. Detailed synthetic procedures and NMR spectra of purified compounds are provided in the Supporting Information.

### Activity profiling of reactivators

**Determination of IC<sub>50</sub>-values:** Dose-response curves and IC<sub>50</sub> values for oximes 7a–e and 8a–e binding to recombinantly expressed apo hAChE were determined with an Ellman assay<sup>[70]</sup> as previously described.<sup>[85]</sup>

**Determination of k<sub>obs</sub> values at 1, 10 and 50 µM:** The reactivation potency of 7a–e and 8a–e towards OPNA-hAChE was assessed by determining k<sub>obs</sub> at oxime concentrations of 1, 10 and 50 µM (Table S4 and Figure S5). Acetylthiocholine iodide (ATCh) and 5,5'-dithio-bis-2-nitrobenzoic acid (DTNB, Ellman's reagent) were purchased from Sigma-Aldrich (Taufkirchen, Germany). The organophosphorus nerve agents tabun, sarin, cyclosarin, VX, and RVX (> 95% by GC-MS. <sup>1</sup>H NMR and <sup>31</sup>P NMR) were made available by the

German Ministry of Defence (Bonn, Germany). All other chemicals were from Merck Eurolab GmbH (Darmstadt, Germany) at the purest grade available. Nerve agent stock solutions (0.1% v/v) were prepared in acetonitrile, stored at room temperature, and diluted appropriately in distilled water immediately before use. Oxime stocks and working solutions were prepared in 50% DMSO in distilled water.

Hemoglobin-free erythrocyte ghosts served as a source of human erythrocyte acetylcholinesterase (AChE) and were prepared as described previously.<sup>[86]</sup> Prior to use, thawed erythrocyte ghosts were homogenised on ice with a Sonoplus HD 2070 ultrasonic homogeniser (Bandelin electronic, Berlin, Germany) twice for 5 s with a 20 s interval in between to achieve a homogenous matrix for kinetic studies.

Inhibited AChE was prepared by adding a small volume (< 1% v/v) of tabun, structure-activity relationshipin, cyclostructure-activity relationshipin, VX, or RVX to erythrocyte ghosts, followed by incubation for 15 min at 37 °C in order to achieve an inhibition of > 95% of control activity. To remove excess OPNA, inhibited samples were dialyzed in phosphate buffer (0.1 M, pH 7.4) overnight at 4 °C and residual enzyme activity was measured by incubation of OPNA-treated and control enzyme samples (30 min, 37 °C). Aliquots were stored at –80 °C until use.

150 µL OPNA-treated AChE was mixed with an equal volume of phosphate buffer (0.1 M, pH 7.4, containing 0.2% gelatin to stabilize AChE). At t = 0, 3 µL oxime (10 µM f.c.) was added to initiate reactivation. After specified time intervals (t = 2–60 min), aliquots were transferred to cuvettes containing phosphate buffer, DTNB (0.3 mM), and ATCh (0.45 mM) and enzyme activity was measured by monitoring absorbance at 412 nm for 3 min.<sup>[70,87]</sup> All experiments were performed in duplicate.

**Data analysis.** Measured AChE activities were used to calculate reactivation percentages using Equation (1).

$$\%reac = \frac{(A_1 - A_i)}{(A_0 - A_i)} \quad (1)$$

Here, A<sub>0</sub> is control AChE activity, A<sub>i</sub> is OP-inhibited AChE activity, and A<sub>1</sub> is oxime reactivated AChE activity. The first order reactivation rate constants (k<sub>obs</sub>) were determined by non-linear regression analysis using GraphPad Prism.

**Determination of pK<sub>a</sub>:** The pK<sub>a</sub> values of oximes 7a–e and 8a–e were determined together with those of HI-6 and obidoxime as references (Table S5). The pK<sub>a</sub> measurements were performed on a Sirius T3 automated instrument from Sirius Analytical Ltd. (East Sussex, UK) equipped with a D-PS (dip probe absorption spectroscopy) lamp for spectrophotometric titrations and a pH electrode for potentiometric titrations. The spectrophotometric titrations were performed using 10 mM stock solutions of the oximes in DMSO, of which 2–5 µL was added to 25 µL of phosphate buffer. The phosphate buffer is added because the amount of sample used was insufficient to act as its own buffering system during the titration. The potentiometric titrations require at least 10-fold higher concentrations, so solid samples or strong DMSO/methanol stock solutions (50–100 mM) can be used. The typical concentration to aim for is > 300 µM (1.5 mL volume) with less than 10 µL DMSO added. Note that no phosphate buffer is added in these titrations. If solubility does not permit, these titrations can be performed using methanol as a co-solvent; the methanol content can be varied between 20–50% wt/wt. During the titration the instrument will add a predetermined volume of ionic-strength-adjusted (ISA) water, or a combination of ISA and ISA containing 80% methanol in the potentiometric titrations. Titrations can be performed between

pH 2 and pH 12, going from high to low or low to high. During the titration, the instrument records the UV-vis spectrum of the sample and uses the D-PS technique to establish a titration curve. In the potentiometric method, the instrument instead bases the titration on the amount of acid (HCl) and base (KOH) that is added. The electrode was calibrated using a blank titration from pH 1.8 to pH 12.0 before every individual determination. The measurements were performed under argon to minimise the effect of dissolved CO<sub>2</sub>. Precipitation was continuously monitored at 500 nm. The temperature was maintained at 25 ± 1 °C throughout the experiment.

**Reactivation kinetics of 7d:** The dissociation and rate constants ( $K_D$  and  $k_r$ ) and the second order rate constant ( $k_{r2}$ ), were determined for **7d** using recombinant hAChE inhibited by a set of five OPNAs. The experiments were performed using a previously reported method.<sup>[58]</sup> A 100 mM stock solution of **7d** was prepared in DMSO and all further dilutions was done in assay buffer. Plots and the used concentration intervals are shown in Figure S6.

**Pre-equilibrium kinetics:** The association and dissociation rate constants were determined using a Kinet Asyst SF-61DX2 stopped-flow instrument (TgK Scientific, Bradford-on-Avon, UK). All measurements were performed using an enzyme concentration of 50 nM in 0.1 M phosphate buffer (pH 7.4) at a temperature of 5 °C. The decay of the fluorescence signal was followed using an excitation wavelength of 276 nm and an emission wavelength of 320 nm. The concentrations of **7d** ranged between 150–800 nM for the rapid binding phase and 0.5–20 μM for the slow phase, with the exact range depending on the OPNA bound to the enzyme (Figures 6 and 7, and S7). The total measuring time varied between 20 ms and 1 s. It should be noted that some of the decay curves for the slow binding site start at a fluorescence intensity that is less than 100% of that for the control sample. This is due to rapid association during the instrument's dead time of 5 ms. Second-order association ( $k_{on}$ ) and dissociation ( $k_{off}$ ) rate constants were obtained as the slopes and ordinate intercepts of linear plots of the observed first order rate constants ( $k_{obs}$ ) as functions of the ligand concentration.

**Molecular modelling of the oxime moiety:** The protein preparation wizard<sup>[88–89]</sup> implemented in Maestro<sup>[90]</sup> was used to prepare four all-atom protein models starting from the X-ray crystal structure of **7d** in complex with tabun-mAChE. His447 was in the A conformation in these models; both neutral and cationic tautomers were considered. The preparation steps included adding hydrogen atoms, creating disulfide bonds, and removing atoms except for the A monomer, the ligand, and water molecules within 5 Å of the remaining heavy atoms. The hydrogens were fully energy minimised in the gas phase using the MMFF94s force field as implemented in MacroModel<sup>[91]</sup> while all heavy atoms were allowed to deviate by up to 0.2 Å from the initial coordinates before a force of 100 kcal/mol Å<sup>2</sup> was applied (constrained energy minimization).

Conformations of the part of **7d** not modelled in the X-ray crystal structure were generated by performing a conformational search in MacroModel using the OPLS2005 force field in the gas phase. During the conformational search, the peripheral fragment including the amide (Figure S11) was fixed and the conformational space of the linker and pyridinium oxime in the catalytic site was searched. The energy window for the generated conformations was set to 15 kcal/mol and the RMSD cutoff for redundant conformers was set to 1 Å. The number of output conformations was set to 100. Conformations of both the protonated and deprotonated oxime of **7d** were generated in the binding site of the protein structures, yielding 56 conformations that were visually analysed.

From the 56 generated conformations of **7d**, 3 were selected for further study: one where the protonated oxime is oriented towards

neutral His447, one where the deprotonated oxime is oriented towards protonated His447, and one where the deprotonated oxime is oriented towards tabun. The complexes representing the three conformations were subjected to constrained energy minimization and the systems were then reduced (Table S8), resulting in models consisting of 436 atoms. The heavy atoms at the truncation sites were replaced with hydrogen atoms that were fully energy minimised in gas phase using the MMFF94s force field in MacroModel while freezing the Cartesian coordinates of the system's remaining atoms. An additional water molecule that was not modelled in the deposited PDB was included in the reduced models.

The reduced atomic systems were subjected to geometry optimization by DFT using the quantum chemical cluster approach.<sup>[92,93]</sup> Geometry optimizations were performed using the DFT functional BLYP in conjunction with the dispersion-accounting method D3 and the 6–31G\*\* basis set as implemented in Jaguar.<sup>[94,95]</sup> The medium grid density option was used and self-consistent field (SCF) calculations were run at the quick level. Direct inversion of the iterative subspace (DIIS)<sup>[96]</sup> was used as convergence method, with the maximum number of SCF iterations set to 48. The energy and RMS density matrix change were set to 5 × 10<sup>−5</sup> and 5 × 10<sup>−6</sup> Hartree, respectively. No solvent model was used. A subset of the atoms were fully flexible during the geometry optimizations (Table S8); the remaining atoms were constrained in the x-, y-, z-coordinates obtained from the constrained force field minimization of the complex including the conformation of **7d** generated in the MacroModel conformational search. The calculations were run at the High Performance Computing Center North (HPC2N).<sup>[97]</sup>

## Acknowledgements

We thank Drs. Mikael Hillgren and Weixing Qian for valuable inputs concerning organic synthesis. The Swedish National Infrastructure for Computing (SNIC) and the High Performance Computing Center North (HPC2N) are acknowledged for computational resources. We acknowledge Dr. Ana Gonzales and the MAX IV Laboratory for time on Beamline Biomax under Proposal 20210533. Research conducted at MAX IV, a Swedish national user facility, is supported by the Swedish Research Council under contract 2018-07152, the Swedish Governmental Agency for Innovation Systems under contract 2018-04969, and Formas under contract 2019-02496. This work was funded by grants from the Swedish Research Council (2018-05176) and by the Swedish Ministry of Defence. NH is funded by the Industrial Doctoral School for Research and Innovation at Umeå University and by the Swedish Defence Research Agency (FOI).

## Conflict of Interest

The authors declare no conflict of interest.

## Data Availability Statement

The data that support the findings of this study are available in the supplementary material of this article.

**Keywords:** drug design · kinetics · nerve agent antidotes · reaction mechanisms · structural biology

- [1] Organisation for the prohibition of chemical weapons; <https://www.opcw.org/chemical-weapons-convention> (August 16, 2021).
- [2] F. Worek, T. Wille, M. Koller, H. Thiermann, *Arch. Toxicol.* **2016**, *90*, 2131–2145.
- [3] F. Worek, H. Jenner, H. Thiermann, *Chemical warfare toxicology: volume 2: management of poisoning* **2016**.
- [4] F. Worek, H. Thiermann, L. Szinicz, P. Eyer, *Biochem. Pharmacol.* **2004**, *68*, 2237–2248.
- [5] K. Sakurada, K. Matsubara, K. Shimizu, H. Shiono, Y. Seto, K. Tsuge, M. Yoshino, I. Sakai, H. Mukoyama, T. Takatori, *Neurochem. Res.* **2003**, *28*, 1401–1407.
- [6] D. E. Lorke, H. Kalasz, G. A. Petroianu, K. Tekes, *Curr. Med. Chem.* **2008**, *15*, 743–753.
- [7] F. Worek, H. Thiermann, T. Wille, *Arch. Toxicol.* **2020**, *94*, 2275–2292.
- [8] N. Maček Hrvat, T. Zorbaz, G. Šinko, Z. Kovarik, *Toxicol. Lett.* **2018**, *293*, 222–228.
- [9] F. Worek, H. Thiermann, *Pharmacol. Ther.* **2013**, *139*, 249–259.
- [10] F. Worek, H. Thiermann, T. Wille, *Chem.-Biol. Interact.* **2016**, *259*, 93–98.
- [11] J. Sussman, M. Harel, F. Frolov, C. Oefner, A. Goldman, L. Toker, I. Silman, *Science* **1991**, *253*, 872–879.
- [12] J. R. McGuire, S. M. Bester, M. A. Guelta, J. Cheung, C. Langley, M. D. Winemiller, S. Y. Bae, V. Funk, J. M. Myslinski, S. D. Pegan, J. J. Height, *Chem. Res. Toxicol.* **2021**, *34*, 804–816.
- [13] S. M. Bester, M. A. Guelta, J. Cheung, M. D. Winemiller, S. Y. Bae, J. Myslinski, S. D. Pegan, J. J. Height, *Chem. Res. Toxicol.* **2018**, *31*, 1405–1417.
- [14] O. Gerlits, X. Kong, X. Cheng, T. Wymore, D. K. Blumenthal, P. Taylor, Z. Radić, A. Kovalevsky, *J. Biol. Chem.* **2019**, *294*, 10607–10618.
- [15] E. N. Carletti, H. Li, B. Li, F. Ekström, Y. Nicolet, M. L. Liodice, E. Gillon, M. T. Froment, O. Lockridge, L. M. Schopfer, P. Masson, F. Nachon, *J. Am. Chem. Soc.* **2008**, *130*, 16011–16020.
- [16] E. Artursson, P. O. Andersson, C. Akfur, A. Linusson, S. Börjegen, F. Ekström, *Biochem. Pharmacol.* **2013**, *85*, 1389–1397.
- [17] I. B. Wilson, S. Ginsburg, *Biochim. Biophys. Acta* **1955**, *18*, 168–170.
- [18] A. F. Childs, D. R. Davies, A. L. Green, J. P. Rutland, *Br. J. Pharmacol. Chemother.* **1955**, *10*, 462–465.
- [19] A. L. Green, H. J. Smith, *Biochem. J.* **1958**, *68*, 28–31.
- [20] A. L. Green, H. J. Smith, *Biochem. J.* **1958**, *68*, 32–35.
- [21] I. B. Wilson, S. Ginsburg, *Biochem. Pharmacol.* **1958**, *1*, 200–206.
- [22] A. J. Franjesevic, S. B. Sillart, J. M. Beck, S. Vyas, C. S. Callam, C. M. Hadad, *Chem. Eur. J.* **2019**, *25*, 5337–5371.
- [23] R. Odzak, M. Calic, T. Hrenar, I. Primozic, Z. Kovarik, *Toxicology* **2007**, *233*, 85–96.
- [24] K. Musilek, J. Kučera, D. Jun, V. Dohnal, V. Opletalova, K. Kuča, *Bioorg. Med. Chem.* **2008**, *16*, 8218–8223.
- [25] J. Kim, Y. R. Malpani, J. Lee, J. S. Shin, S. B. Han, Y.-S. Jung, *Bioorg. Med. Chem. Lett.* **2018**, *28*, 3784–3786.
- [26] S. B. Bharate, C.-K. Chao, C. M. Thompson, *Environ. Toxicol. Pharmacol.* **2019**, *71*, 103218.
- [27] J. Acharya, H. Rana, V. A. Kapil, M. P. Kaushik, *Med. Chem. Res.* **2013**, *22*, 1277–1286.
- [28] K. Kuča, J. Bielavský, J. Cabal, J. Kassa, *Bioorg. Med. Chem. Lett.* **2003**, *13*, 3545–3547.
- [29] K. Musilek, O. Holas, K. Kuča, D. Jun, V. Dohnal, M. Dolezal, *Bioorg. Med. Chem. Lett.* **2006**, *16*, 5673–5676.
- [30] K. Musilek, M. Komloova, O. Holas, A. Horova, M. Pohanka, F. Gunn-Moore, V. Dohnal, M. Dolezal, K. Kuča, *Bioorg. Med. Chem.* **2011**, *19*, 754–762.
- [31] K. Musilek, O. Holas, K. Kuča, D. Jun, V. Dohnal, M. Dolezal, *J. Enzyme Inhib. Med. Chem.* **2007**, *22*, 425–432.
- [32] K. Musilek, D. Jun, J. Cabal, J. Kassa, F. Gunn-Moore, K. Kuča, *J. Med. Chem.* **2007**, *50*, 5514–5518.
- [33] J. Acharya, A. K. Gupta, D. K. Dubey, S. K. Raza, *Eur. J. Med. Chem.* **2009**, *44*, 1335–1340.
- [34] J. Acharya, D. K. Dubey, S. K. Raza, *Toxicol. in Vitro* **2010**, *24*, 1797–1802.
- [35] J. Acharya, D. K. Dubey, A. K. Srivastava, S. K. Raza, *Toxicol. in Vitro* **2011**, *25*, 251–256.
- [36] Z. Kovarik, J. Kalisiak, N. M. Hrvat, M. Katalinić, T. Zorbaz, S. Žunec, C. Green, Z. Radić, V. V. Fokin, K. B. Sharpless, P. Taylor, *Chem. Eur. J.* **2019**, *25*, 4100–4114.
- [37] H. N. Karade, A. K. Valiveti, J. Acharya, M. P. Kaushik, *Bioorg. Med. Chem.* **2014**, *22*, 2684–2691.
- [38] T.-M. Shih, J. W. Skovira, J. C. O'Donnell, J. H. McDonough, *J. Mol. Neurosci.* **2010**, *40*, 63–69.
- [39] G. Mercey, T. Verdelet, G. Saint-André, E. Gillon, A. Wagner, R. Baati, L. Jean, F. Nachon, P.-Y. Renard, *Chem. Commun.* **2011**, *47*, 5295–5297.
- [40] R. K. Sit, Z. Radić, V. Gerardi, L. Zhang, E. Garcia, M. Katalinić, G. Amitai, Z. Kovarik, V. V. Fokin, K. B. Sharpless, P. Taylor, *J. Biol. Chem.* **2011**, *286*, 19422–19430.
- [41] M. C. de Koning, M. van Grol, D. Noort, *Toxicol. Lett.* **2011**, *206*, 54–59.
- [42] G. Saint-Andre, M. Kliachyna, S. Kodepelly, L. Louise-Leriche, E. Gillon, P.-Y. Renard, F. Nachon, R. Baati, A. Wagner, *Tetrahedron* **2011**, *67*, 6352–6361.
- [43] J. Kalisiak, E. C. Ralph, J. R. Cashman, *J. Med. Chem.* **2012**, *55*, 465–474.
- [44] L. Gorecki, O. Gerlits, X. Kong, X. Cheng, D. K. Blumenthal, P. Taylor, C. Ballatore, A. Kovalevsky, Z. Radić, *J. Biol. Chem.* **2020**, jbc.RA119.01240.
- [45] G. Santoni, J. De Sousa, E. De La Mora, J. Dias, L. Jean, J. L. Sussman, I. Silman, P.-Y. Renard, R. C. D. Brown, M. Weik, R. Baati, F. Nachon, *J. Med. Chem.* **2018**, *61*, 7630–7639.
- [46] I. V. Khavrutskii, A. Wallqvist, *ChemistrySelect* **2017**, *2*, 1885–1890.
- [47] M. C. De Koning, G. Horn, F. Worek, M. Van Grol, *Eur. J. Med. Chem.* **2018**, *157*, 151–160.
- [48] H. C. Jeong, N. S. Kang, N.-J. Park, E. K. Yum, Y.-S. Jung, *Bioorg. Med. Chem. Lett.* **2009**, *19*, 1214–1217.
- [49] H. C. Jeong, N.-J. Park, C. H. Chae, K. Musilek, J. Kassa, K. Kuča, Y.-S. Jung, *Bioorg. Med. Chem.* **2009**, *17*, 6213–6217.
- [50] T. Zorbaz, D. Malinak, N. Maraković, N. M. Hrvat, A. Zandona, M. Novotny, A. Skarka, R. Andrys, M. Benkova, O. Soukup, M. Katalinić, K. Kuča, Z. Kovarik, K. Musilek, *J. Med. Chem.* **2018**, *61*, 10753–10766.
- [51] G. E. Garcia, A. J. Campbell, J. Olson, D. Moorad-Doctor, V. I. Morthole, *Chem.-Biol. Interact.* **2010**, *187*, 199–206.
- [52] J. C. DeMar, E. D. Clarkson, R. H. Ratcliffe, A. J. Campbell, S. G. Thangave-lu, C. A. Herdman, H. Leader, S. M. Schulz, E. Marek, M. A. Medynets, T. C. Ku, S. A. Evans, F. A. Khan, R. R. Owens, M. P. Nambiar, R. K. Gordon, *Chem.-Biol. Interact.* **2010**, *187*, 191–198.
- [53] H. Rice, T. M. Mann, S. J. Armstrong, M. E. Price, A. C. Green, J. E. H. Tattersall, *Chem.-Biol. Interact.* **2016**, *259*, 175–181.
- [54] F. Ekström, A. Hörnberg, E. Artursson, L.-G. Hammarström, G. Schneider, Y.-P. Pang, *PLoS One* **2009**, *4*, e5957.
- [55] B. J. Bennion, S. G. Essiz, E. Y. Lau, J.-L. Fattebert, A. Emigh, F. C. Lightstone, *PLoS One* **2015**, *10*, e0121092.
- [56] J. Peters, N. Martinez, M. Trovaslet, K. Scannapieco, M. M. Koza, P. Masson, F. Nachon, *Phys. Chem. Chem. Phys.* **2016**, *18*, 12992–13001.
- [57] F. J. Ekström, C. Åstot, Y. P. Pang, *Clin. Pharmacol. Ther.* **2007**, *82*, 282–293.
- [58] A. Allgardsson, L. Berg, C. Akfur, A. Hörnberg, F. Worek, A. Linusson, F. Ekström, *Proc. Natl. Acad. Sci. USA* **2016**, *113*, 5514–5519.
- [59] C. D. Andersson, J. M. Hillgren, C. Lindgren, W. Qian, C. Akfur, L. Berg, F. Ekström, A. Linusson, *J. Comput.-Aided Mol. Des.* **2015**, *29*, 199–215.
- [60] Y.-P. Pang, T. M. Kollmeyer, F. Hong, J.-C. Lee, P. I. Hammond, S. P. Haugabouk, S. Brimijoin, *Chem. Biol.* **2003**, *10*, 491–502.
- [61] R. A. Copeland, D. L. Pompliano, T. D. Meek, *Nat. Rev. Drug Discovery* **2006**, *5*, 730–739.
- [62] R. A. Copeland, *Nat. Rev. Drug Discovery* **2016**, *15*, 87–95.
- [63] Z. Radić, P. Taylor, *J. Biol. Chem.* **2001**, *276*, 4622–4633.
- [64] Z. Radić, J. Kalisiak, V. V. Fokin, K. B. Sharpless, P. Taylor, *Chem.-Biol. Interact.* **2010**, *187*, 163–166.
- [65] C. B. Millard, G. Kryger, A. Ordentlich, H. M. Greenblatt, M. Harel, M. L. Raves, Y. Segall, D. Barak, A. Shafferman, I. Silman, J. L. Sussman, *Biochemistry* **1999**, *38*, 7032–7039.
- [66] S. Knutsson, C. Engdahl, R. Kumari, N. Forsgren, C. Lindgren, T. Kindahl, S. Kitur, L. Wachira, L. Kamau, F. Ekström, A. Linusson, *J. Med. Chem.* **2018**, *61*, 10545–10557.
- [67] S. Knutsson, T. Kindahl, C. Engdahl, D. Nikjoo, N. Forsgren, S. Kitur, F. Ekström, L. Kamau, A. Linusson, *Eur. J. Med. Chem.* **2017**, *134*, 415–427.
- [68] R. Appel, *Angew. Chem. Int. Ed.* **1975**, *14*, 801–811; *Angew. Chem.* **1975**, *87*, 863–874.
- [69] S. Ginsburg, I. B. Wilson, *J. Am. Chem. Soc.* **1957**, *79*, 481–485.
- [70] G. L. Ellman, K. D. Courtney, V. Andres, R. M. Featherstone, *Biochem. Pharmacol.* **1961**, *7*, 88.
- [71] E. Artursson, C. Akfur, A. Hörnberg, F. Worek, F. Ekström, *Toxicology* **2009**, *265*, 108–114.
- [72] T. Wille, F. Ekström, J.-C. Lee, Y.-P. Pang, H. Thiermann, F. Worek, *Biochem. Pharmacol.* **2010**, *80*, 941–946.

- [73] B. Velan, H. Grosfeld, C. Kronman, M. Leitner, Y. Gozes, A. Lazar, Y. Flashner, D. Marcus, S. Cohen, A. Shafferman, *J. Biol. Chem.* **1991**, 266, 23977–23984.
- [74] A. Hörnberg, A.-K. Tunemalm, F. Ekström, *Biochemistry* **2007**, 46, 4815–4825.
- [75] R. Lo, N. B. Chandar, M. K. Kesharwani, A. Jain, B. Ganguly, *PLoS One* **2013**, 8, e79591.
- [76] T. Driant, F. Nachon, C. Ollivier, P.-Y. Renard, E. Derat, *ChemBioChem* **2017**, 18, 666–675.
- [77] J. Jończyk, J. Kukułowicz, K. Łątka, B. Malawska, Y.-S. Jung, K. Musilek, M. Bajda, *Biomol. Eng.* **2021**, 11, 169.
- [78] F. R. D. Souza, D. Rodrigues Garcia, T. Cuya, A. S. Pimentel, A. D. S. Gonçalves, R. B. D. Alencastro, T. C. C. França, *ACS Omega* **2020**, 5, 4490–4500.
- [79] F. Ekström, C. Akfur, A.-K. Tunemalm, S. Lundberg, *Biochemistry* **2006**, 45, 74–81.
- [80] F. Ekström, Y.-P. Pang, M. Boman, E. Artursson, C. Akfur, S. Börjegen, *Biochem. Pharmacol.* **2006**, 72, 597–607.
- [81] W. Kabsch, *Acta Crystallogr. Sect. D* **2010**, 66, 125–132.
- [82] M. D. Winn, C. C. Ballard, K. D. Cowtan, E. J. Dodson, P. Emsley, P. R. Evans, R. M. Keegan, E. B. Krissinel, A. G. W. Leslie, A. McCoy, S. J. McNicholas, G. N. Murshudov, N. S. Pannu, E. A. Potterton, H. R. Powell, R. J. Read, A. Vagin, K. S. Wilson, *Acta Crystallogr. Sect. D* **2011**, 67, 235–242.
- [83] P. D. Adams, P. V. Afonine, G. Bunkóczi, V. B. Chen, I. W. Davis, N. Echols, J. J. Headd, L.-W. Hung, G. J. Kapral, R. W. Grosse-Kunstleve, A. J. McCoy, N. W. Moriarty, R. Oeffner, R. J. Read, D. C. Richardson, J. S. Richardson, T. C. Terwilliger, P. H. Zwart, *Acta Crystallogr. Sect. D* **2010**, 66, 213–221.
- [84] P. Emsley, B. Lohkamp, W. G. Scott, K. Cowtan, *Acta Crystallogr. Sect. D* **2010**, 66, 486–501.
- [85] L. Berg, C. D. Andersson, E. Artursson, A. Hörnberg, A.-K. Tunemalm, A. Linusson, F. Ekström, *PLoS One* **2011**, 6, e26039.
- [86] F. Worek, T. Wille, M. Koller, H. Thiermann, *Biochem. Pharmacol.* **2012**, 83, 1700–1706.
- [87] F. Worek, U. Mast, D. Kiderlen, C. Diepold, P. Eyer, *Clin. Chim. Acta* **1999**, 288, 73–90.
- [88] Schrödinger Release 2019–1: Protein Preparation Wizard; Epik, Schrödinger, LLC, New York, NY, 2019; Impact, Schrödinger, LLC, New York, NY, 2019; Prime, Schrödinger, LLC, New York, NY, 2019.
- [89] G. Madhavi Sastry, M. Adzhigirey, T. Day, R. Annabhimoju, W. Sherman, *J. Comput.-Aided Mol. Des.* **2013**, 27, 221–234.
- [90] Schrödinger Release 2019–1: Maestro, Schrödinger, LLC, New York, NY, 2019.
- [91] Schrödinger Release 2014–1: MacroModel, Schrödinger, LLC, New York, NY, 2014.
- [92] P. E. M. Siegbahn, F. Himo, *J. Biol. Inorg. Chem.* **2009**, 14, 643–651.
- [93] P. E. M. Siegbahn, F. Himo, *Interdiscip. Rev. Comput. Mol. Sci.* **2011**, 1, 323–336.
- [94] Schrödinger Release 2014–1: Jaguar, Schrödinger, LLC, New York, NY, 2014.
- [95] A. D. Bochevarov, E. Harder, T. F. Hughes, J. R. Greenwood, D. A. Braden, D. M. Philipp, D. Rinaldo, M. D. Halls, J. Zhang, R. A. Friesner, *Int. J. Quantum Chem.* **2013**, 113, 2110–2142.
- [96] E. D. Glendening, J. K. Badenhoop, A. E. Reed, J. E. Carpenter, J. A. Bohmann, C. M. Morales, C. R. Landis, F. Weinhold, <http://nbo6.chem.wisc.edu/>.
- [97] High Performance Computer Center North (HPC2 N). <http://www.hpc2n.umu.se/>.

Manuscript received: March 2, 2022  
Accepted manuscript online: April 14, 2022  
Version of record online: June 7, 2022